Forward Electron Identification in 1.96-TeV Proton-Antiproton Collisions

（重心系エネルギー 1.96TeV 陽子・反陽子衝突実験における前方領域の電子同定）

理学研究科

数物系専攻

大和　大祐

Forward Electron Identification in 1.96-TeV Proton-Antiproton Collisions

A dissertation submitted
in partial fullfillment of the requirements
for the Degree of Master of Philosophy in Science
in the Graduate School of Science of
Osaka City University

by
Daisuke Yamato

February 14th, 2011

Abstract

In particle physics, the Standard Model (SM) is believed as the law to describe fundamental particles to some extent. However, the Higgs boson, which contributes to giving masses to fermions and bosons without violating the gauge invariance in the SM, has not been discovered yet. Many particle experimentalists in the world are working hard to search for it. If we can detect, the missing link in the SM is solved, and then we can progress to the next step with the firm basis. Otherwise, that is, the Higgs boson is confirmed that it does not exist, it is time to consider an alternative theory beyond the SM.

This thesis describes a study of the forward electron (pseudorapidity η satisfies $1.1 < |\eta| < 2.0$ region) identification in $\sqrt{s} = 1.96$ TeV proton-antiproton collisions. The motivation stems from incorporating this to the search for the $Wh \rightarrow WWW$ process by using like-sign dilepton events. Now at CDF, Collider Detector at Fermilab, increasing acceptance tends to decrease the limit of the cross section for Higgs production. The previous result used only the leptons in the central region ($|\eta| < 1.0$). Therefore, we think that using the central plus forward leptons could deduce better result than the previous.

Although increasing the acceptance geometrically results in attracting the signal, it also increases more backgrounds. Even worse, in the forward region, there are poorer detectors to identify leptons than the central region. Therefore, effective selections for signal events is the key to use the forward region and to search for the Higgs boson.

The previous result by using likelihood-based lepton identification (LLID) in the central region shows better performance than the cut-based method which is commonly used at CDF. Therefore, we apply the LLID to the forward electrons, and compare the performance with the cut-based method. Furthermore, the plug pre-shower (PPR) detector information, which is not used in the cut-based method, is applied to the LLID for more separation between the signal and backgrounds.

We choose Z Monte Carlo samples as the signal probability distribution function (PDF) and jet samples as the background PDF, and find that the LLID background reduction factor is about 3.5 times larger than the CLID with fixing the same signal efficiency.

Also, in this thesis, it describes the matrix element method, which is the powerful method to discriminate the signal from backgrounds by using the all kinematical information. Especially, we think that the $WZ/ZZ \rightarrow$ like-sign dilepton irreducible backgrounds can be rejected by this method to some extent. This method is, however,

complicated in $Wh \rightarrow WWW$ because of various difficulties from 4 missing particles, interpretation of transfer functions, which is the bridge between the detector information and parton information, numerical integration, and so on. Here, we explain the method as plan, and are going to incorporate this in the near future.

Acknowledgment

I enjoyed studying the particle physics, analyzing the CDF data with sophisticated constituents, and discussing many people related to the CDF experiment.

I would like to express my thankful feelings to Professor Yoshihiro Seiya, who kept supporting and encouraging me to study this analysis, and brought me to the good restaurant frequently. I also need to thank Professor Kazuhiro Yamamoto, who was throwing doubt on my story in the meetings and then I got the oppotunity to think the arguments deeply.

I am great thankful to Takayuki Wakisaka. He is very understanding me and taught me the basis of my analysis from scratch because I had been studied particle physics only from the view of the theory. And I spent the fruitful time to discuss him about my analysis, and small talks! I am also grateful to Atsunari Hamaguchi for advising and supporting me to live in the Fermilab with great time.

In my staying at Fermilab, I encountered many people to support me. Especially, I would like to thank shift crews during the same period, Joe Boudreau, Fabrizio Ruffini, Azeddine Kasmi, Silvia Amerio, and Mark Mattson. They are very kind to me and supported me whenever I encountered a trouble. Also, I am thankful to Francesco Devoto and Joulien Tater, who are the owl and day consumer operator shift in my shift days. I am enjoying with them to send e-mails each other even after ending the shifts, and expect to continue this good relation.

Finally, I have to say thank my family. They provided me the financial support and warm house and meals every day.

Contents

List of Figures

List of Tables

Chapter 1

Introduction

Physics have been developed by many, many people for the purpose of investigation for nature. Newton constituted the basic of physics, mechanics, which describes the point of mass; Maxwell collected up various theory for electromagnetics, which brings the important idea *"field"*; Schrödinger and Heisenberg produced the bases of quantum mechanics independently, which tells us how dwellers live in the small world, and Dirac integrated these; Einstein wrote two papers: one is Special Relativity, which explains the movement of an object having extreme speed, and the otheer is general relativity, which modified the Newton's law and predicted the gravitational waves (These are not detected directly. I hope reseachers find them in the "near" future!)

In particle physics, people think the Standard Model (SM) tells how the small constituents of matters move and interact to some extent. However, the particles are basically massless because the Standard Model stems from the gauge theory. The candidate for the acceptable mass generation theory exists, and is called the *"Higgs mechanism"*. Theorists have generated some theory for Grand Unifition Theory, e.g. SUperSYmmetry (SUSY, [2], [3]), and some of them have the root of the Higgs mechanism. However, the *"higgs boson"* predicted by the theory has not been discovered yet now. Therefore, this search is very important for particle physics; if the higgs boson exists, we will get the strong foundation; and if not exists, we will get the oppotunity to consider the alternative theory for generating mass of particles, and may arrive the entrance for the new physics!

1.1 Abelian Gauge Theory

1.1.1 Global U(1) Symmetry

Before the introduction for the Standard Model, I introduce some basic theory. Here, I explain briefly, so if you want to know more, please read some materials (e.g. [4, 5, 6, 7, 8]).

Consider the system which has one complex free scalar field with mass M. The Lagrangian is (More precisely, this means Lagrangian density. However, I also call it

Lagrangian for simplicity, and you can distinguish these by the letter: Lagrangian is L and the Lagrangian density is $\mathcal{L}$)

$$\hat{\mathcal{L}} = \partial_\mu \hat{\phi}^\dagger \partial^\mu \hat{\phi} - M^2 \hat{\phi}^\dagger \hat{\phi} \tag{1.1}$$

and the Hamiltonian is (with dropping the zero-point energy)

$$\hat{H} = \int \frac{\mathrm{d}^3 \boldsymbol{k}}{(2\pi)^3} [\hat{a}^\dagger(k)\hat{a}(k) + \hat{b}^\dagger(k)\hat{b}(k)]\omega, \tag{1.2}$$

where ϕ is the complex scalar field and can be expanded as

$$\hat{\phi} = \int \frac{\mathrm{d}^3 \boldsymbol{k}}{(2\pi)^3 \sqrt{2\omega}} [\hat{a}(k)e^{-ik\cdot x} + \hat{b}^\dagger(k)e^{ik\cdot x}]. \tag{1.3}$$

Note that ϕ and $\phi^\dagger$ behave independently. This Lagrangian is invariant under the transformation

$$\hat{\phi}' = e^{-i\alpha}\hat{\phi}, \tag{1.4}$$

where α is some constant. (1.4) is called a global U(1) phase transformation and we say *"this Lagrangian has U(1) symmetry"*.

If Lagrangian has such a symmetry, we can deduce some important quantity. Because this Lagrangian is invariant under (1.4),

$$0 = \delta\hat{\mathcal{L}} = \frac{\partial\hat{\mathcal{L}}}{\partial(\partial_\mu\hat{\phi})}\delta(\partial_\mu\hat{\phi}) + \frac{\partial\hat{\mathcal{L}}}{\partial(\partial_\mu\hat{\phi}^\dagger)}\delta(\partial_\mu\hat{\phi}^\dagger) + \frac{\partial\hat{\mathcal{L}}}{\partial\hat{\phi}}\delta\hat{\phi} + \frac{\partial\hat{\mathcal{L}}}{\partial\hat{\phi}^\dagger}\delta\hat{\phi}^\dagger \tag{1.5}$$

With the help of the equations of motion, $\delta\mathcal{L}$ is rewritten as

$$\delta\hat{\mathcal{L}} = \frac{\partial\hat{\mathcal{L}}}{\partial(\partial_\mu\hat{\phi})}\delta(\partial_\mu\hat{\phi}) + \frac{\partial\hat{\mathcal{L}}}{\partial(\partial_\mu\hat{\phi}^\dagger)}\delta(\partial_\mu\hat{\phi}^\dagger) + \left[\partial_\mu\left(\frac{\partial\hat{\mathcal{L}}}{\partial(\partial_\mu\hat{\phi})}\right)\right]\delta\hat{\phi} + \left[\partial_\mu\left(\frac{\partial\hat{\mathcal{L}}}{\partial(\partial_\mu\hat{\phi}^\dagger)}\right)\right]\delta\hat{\phi}^\dagger \tag{1.6}$$

Since $\delta(\partial_\mu\hat{\phi}^{(\dagger)}) = \partial_\mu(\delta\hat{\phi}^{(\dagger)})$, (1.5) becomes

$$0 = \partial_\mu\left[\frac{\partial\hat{\mathcal{L}}}{\partial(\partial_\mu\hat{\phi})}\delta\hat{\phi} + \frac{\partial\hat{\mathcal{L}}}{\partial(\partial_\mu\hat{\phi}^\dagger)}\delta\hat{\phi}^\dagger\right] \tag{1.7}$$

Note that the above argument is general and will apply the Lagrangian which has some different symmetry. In this U(1) case, $\delta\hat{\phi}$ and $\delta\hat{\phi}^\dagger$ are (assume α is very tiny quantity)

$$\delta\hat{\phi} = \hat{\phi}' - \hat{\phi} \approx -i\alpha\hat{\phi}, \tag{1.8}$$

$$\delta\hat{\phi}^\dagger = \hat{\phi}'^\dagger - \hat{\phi}^\dagger \approx i\alpha\hat{\phi}^\dagger, \tag{1.9}$$

and (1.7) reduces to

$$\begin{aligned} 0 &= \partial_\mu\left[-\frac{\partial\hat{\mathcal{L}}}{\partial(\partial_\mu\hat{\phi})}i\alpha\hat{\phi} + \frac{\partial\hat{\mathcal{L}}}{\partial(\partial_\mu\hat{\phi}^\dagger)}i\alpha\hat{\phi}^\dagger\right] \\ &= -i\alpha\partial_\mu[(\partial^\mu\hat{\phi}^\dagger)\phi - (\partial^\mu\hat{\phi})\hat{\phi}^\dagger] \end{aligned} \tag{1.10}$$

Since α is arbitrary, we get the result that the 4-vector operator

$$\hat{N}^{\mu}_{\phi} = i(\hat{\phi}^{\dagger}\partial^{\mu}\hat{\phi} - \hat{\phi}\partial^{\mu}\hat{\phi}^{\dagger}) \tag{1.11}$$

is conserved, that is,

$$\partial_{\mu}\hat{N}^{\mu}_{\phi} = 0. \tag{1.12}$$

We call $\hat{N}^{\mu}_{\phi}$ the *symmetry current*. (1.12) is equivalent to

$$\partial\hat{N}^{0}_{\phi}/\partial t + \boldsymbol{\nabla}\cdot\hat{\boldsymbol{N}}_{\phi} = 0 \tag{1.13}$$

Integrating this over all space, we obtain

$$\frac{\mathrm{d}}{\mathrm{d}t}\int_{V\to\infty}\hat{N}^{0}_{\phi}\mathrm{d}^{3}\boldsymbol{x} + \int_{S\to\infty}\hat{\boldsymbol{N}}_{\phi}\cdot\mathrm{d}\boldsymbol{S} = 0, \tag{1.14}$$

where we used the Gauss's theorem in the second term. We often assume that surface integral is zero at the infinity, and we get

$$\frac{\mathrm{d}}{\mathrm{d}t}\int_{V\to\infty}\hat{N}^{0}_{\phi}\mathrm{d}^{3}\boldsymbol{x} = 0. \tag{1.15}$$

Therefore, we can say that the quantity

$$\hat{N}_{\phi} = \int\hat{N}^{0}_{\phi}\mathrm{d}^{3}\boldsymbol{x} \tag{1.16}$$

is the constant in time, where $\hat{N}_{\phi}$ is called the symmetry operator.

The symmetry operator has important properties:

1. $\mathrm{d}\hat{N}_{\phi}/\mathrm{d}t = 0$ (from previous arguments);
2. $[\hat{N}_{\phi}, \hat{H}] = 0$ (from the Heisenberg equation);
3. the symmetry operator relates to the global U(1) transformation, that is,

$$\hat{U}(\alpha)\hat{\phi}\hat{U}^{-1}(\alpha) = e^{-i\alpha}\hat{\phi} = \hat{\phi}' \tag{1.17}$$

with

$$\hat{U}(\alpha) = e^{i\alpha\hat{N}_{\phi}}. \tag{1.18}$$

This can be proven by using

$$[\hat{N}_{\phi}, \hat{\phi}] = -\hat{\phi} \tag{1.19}$$

and

$$[\hat{N}_{\phi}, \hat{\phi}^{\dagger}] = \hat{\phi}^{\dagger}. \tag{1.20}$$

Because $\hat{N}_{\phi}$ determines the form of the infinitesimal transformation of $\hat{U}$, it seems to be good to call it the *generator* of global U(1) transformations ([5], [9]).

We can apply this procedure to the Dirac case. The Dirac Lagrangian is

$$\mathcal{L}_D = \bar{\psi}(i\gamma^\mu \partial_\mu - m)\psi, \tag{1.21}$$

To quantize the field, we expand it as a mode expansion

$$\hat{\psi} = \int \frac{\mathrm{d}^3\boldsymbol{k}}{(2\pi)^3\sqrt{2\omega}} \sum_{s=1,2} [\hat{c}_s(k)u(k,s)e^{-ik\cdot x} + \hat{d}_s^\dagger(k)v(k,s)e^{ik\cdot x}], \tag{1.22}$$

where $\omega = \sqrt{m^2 + \boldsymbol{k}^2}$. This Lagrangian is also invariant under U(1) phase transformation, and we obtain the corresponding symmetry current

$$\hat{N}^\mu_\psi = \bar{\hat{\psi}}\gamma^\mu\hat{\psi} \tag{1.23}$$

and the associated symmetry operator

$$\hat{N}_\psi = \int \hat{\psi}^\dagger\hat{\psi}\mathrm{d}^3\boldsymbol{x}. \tag{1.24}$$

1.1.2 Local U(1) Symmetry

In the previous section, we introduce that Global U(1) transformation is given by 1.4, where α is constant. Local U(1) symmetry is obtained by the replacement

$$\alpha \rightarrow \alpha(x), \tag{1.25}$$

that is, α is not constant, but depends on the location in some coordinates. Of course, the original Lagrangian (1.1) or (1.21) is not invariant under (1.25). However, we can get the invariant Lagrangian with the replacement of ordinal derivatives by the *covariant derivatives*. In the Dirac case, we have the covariant derivative (and with the replacement of α by q, which stands for a *charge*)

$$\partial^\mu \rightarrow \hat{D}^\mu = \partial^\mu + iq\hat{A}^\mu, \tag{1.26}$$

where $\hat{A}$ is the new field and is called a *gauge field*. The Dirac field is invariant under the local U(1) phase transformation

$$\hat{\psi}(\boldsymbol{x},t) \rightarrow \hat{\psi}'(\boldsymbol{x},t) = e^{-iq\hat{\chi}(\boldsymbol{x},t)}\hat{\psi}(\boldsymbol{x},t) \tag{1.27}$$

if the gauge field transforms as

$$\hat{A}^\mu \rightarrow \hat{A}'^\mu = \hat{A}^\mu + \partial^\mu\hat{\chi}. \tag{1.28}$$

This locally U(1)-invariant Lagrangian

$$\hat{\mathcal{L}}_{\text{D local}} = \bar{\psi}(i\gamma^\mu\hat{D}_\mu - m)\psi \tag{1.29}$$

can be thought as

$$\hat{\mathcal{L}}_{\mathrm{D}} \rightarrow \hat{\mathcal{L}}_{\mathrm{D\ local}} = \hat{\mathcal{L}}_{\mathrm{D}} + \hat{\mathcal{L}}_{\mathrm{int}}, \tag{1.30}$$

where

$$\hat{\mathcal{L}}_{\mathrm{int}} = -q\bar{\hat{\psi}}\gamma^{\mu}\hat{\psi}\hat{A}_{\mu}. \tag{1.31}$$

Gauge field appears in $\hat{\mathcal{L}}_{\mathrm{int}}$ term, and therefore, we can interpret it as the force carriers between matter fields.

Up to here, we have obtaind formal steps for Lagrangian with interactions, that is:

1. Find the Lagrangian which has some global symmetry;
2. Modify the Lagrangian satisfying local symmetry. This can be simply obtained by replacing the ordinal derivatives to the covariant ones;
3. Add new gauge field(s) to the covariant derivatives;
4. Expand the covariant derivatives, and you can get the Lagrangian with the gauge interaction(s).

1.2 Non-Abelian Gauge Theory

1.2.1 Global Symmetry

We follow the previous procedure, except for the difference between Abelian and Non-Abelian.

Consider the Lagrangian

$$\hat{\mathcal{L}} = \bar{\hat{u}}(i\partial\!\!\!/ - m)\hat{u} + \bar{\hat{d}}(i\partial\!\!\!/ - m)\hat{d} \tag{1.32}$$

involving two free fermions 'u' and 'd' of equal mass m with the abbreviation of $\hat{u} = \hat{\psi}_u$ and $\hat{d} = \hat{\psi}_d$. For simplicity, using the 2-component notation

$$\hat{q} = \begin{pmatrix} \hat{u} \\ \hat{d} \end{pmatrix}, \tag{1.33}$$

(1.32) can be written as

$$\hat{\mathcal{L}} = \bar{\hat{q}}(i\partial\!\!\!/ - m)\hat{q}. \tag{1.34}$$

This Lagrangian is invariant under global U(1) phase transformation and also global SU(2) transformations acting on the $u - d$ space

$$\hat{q}' = \exp(-i\boldsymbol{\alpha} \cdot \boldsymbol{\tau}/2)\hat{q}, \tag{1.35}$$

where $\boldsymbol{\tau}$ are

$$\tau_1 = \begin{pmatrix} 0 & 1 \\ 1 & 0 \end{pmatrix}, \tau_2 = \begin{pmatrix} 0 & -i \\ i & 0 \end{pmatrix}, \tau_3 = \begin{pmatrix} 1 & 0 \\ 0 & -1 \end{pmatrix}, \tag{1.36}$$

and $\boldsymbol{\alpha} = (\alpha_1, \alpha_2, \alpha_3)$ are constant parameters. ($\boldsymbol{\tau}$ are the same as the Pauli's spin matrices. However, $\boldsymbol{\tau}$ does NOT belong to spin space, so here distinguish each other.) In the infinitesimal case, (1.35) reduces to

$$\hat{q}' = (1 - i\boldsymbol{\epsilon} \cdot \boldsymbol{\tau}/2)\hat{q}, \quad \boldsymbol{\epsilon} = (\epsilon_1, \epsilon_2, \epsilon_3). \tag{1.37}$$

As the U(1) case (there, $\hat{N}_\phi$ as symmetry operator), we can deduce three independent generators

$$\hat{\boldsymbol{T}}^{(\frac{1}{2})} = \left(\hat{T}_1^{(\frac{1}{2})}, \hat{T}_2^{(\frac{1}{2})}, \hat{T}_3^{(\frac{1}{2})}\right) \tag{1.38}$$

such that

$$\hat{q}' = \hat{U}^{(\frac{1}{2})}\hat{q}\hat{U}^{(\frac{1}{2})\dagger} \tag{1.39}$$

and

$$\hat{U}^{(\frac{1}{2})} = \exp(i\boldsymbol{\alpha} \cdot \hat{\boldsymbol{T}}^{(\frac{1}{2})}), \tag{1.40}$$

where $\hat{\boldsymbol{T}}^{(\frac{1}{2})}$ are Hermitian so that $\hat{U}^{(\frac{1}{2})}$ is unitary. In the infinitesimal case, $\hat{\boldsymbol{T}}^{(\frac{1}{2})}$ must satisfy

$$(1 - i\boldsymbol{\epsilon} \cdot \boldsymbol{\tau}/2)\hat{q} = (1 + i\boldsymbol{\epsilon} \cdot \hat{\boldsymbol{T}}^{(\frac{1}{2})})\hat{q}(1 - i\boldsymbol{\epsilon} \cdot \hat{\boldsymbol{T}}^{(\frac{1}{2})}). \tag{1.41}$$

Expanding right hand side, and comparing the coefficients of $\boldsymbol{\epsilon}$ on both sides, then $\hat{\boldsymbol{T}}$ must satisfy

$$[\hat{\boldsymbol{T}}^{(\frac{1}{2})}, \hat{q}] = -(\boldsymbol{\tau}/2)\hat{q}. \tag{1.42}$$

The form of $\hat{\boldsymbol{T}}$ is expected analogous to U(1) case (cf. (1.23) and (1.24)):

$$\hat{\boldsymbol{T}}^{(\frac{1}{2})} = \int \hat{\boldsymbol{T}}^{(\frac{1}{2})0} \mathrm{d}^3\boldsymbol{x} \tag{1.43}$$

and

$$\hat{\boldsymbol{T}}^{(\frac{1}{2})\mu} = \bar{\hat{q}}\gamma^\mu \frac{\boldsymbol{\tau}}{2}\hat{q}. \tag{1.44}$$

The above discussion is expanded to the SU(3) case easily. Consider the Lagrangian

$$\hat{\mathcal{L}} = \bar{\hat{q}}(i\partial\!\!\!/ - m)\hat{q} \tag{1.45}$$

with

$$\hat{q} = \begin{pmatrix} \hat{q}_1 \\ \hat{q}_2 \\ \hat{q}_3 \end{pmatrix}. \tag{1.46}$$

This Lagrangian apparently has the nature of invariance under SU(3) phase transformation

$$\hat{q}' = \exp(-i\boldsymbol{\alpha} \cdot \boldsymbol{\lambda}/2)\hat{q}. \tag{1.47}$$

The symmetry currents are

$$\hat{G}_a^{(q)\mu} = \bar{\hat{q}}\gamma^\mu \frac{\lambda_a}{2}\hat{q}, a = 1, 2, \ldots, 8, \tag{1.48}$$

and the associated symmetry operators are

$$\hat{G}_a^{(q)} = \int \hat{G}_a^{(q)0} \mathrm{d}^3\boldsymbol{x} = \int \hat{q}^\dagger \frac{\lambda_a}{2} \hat{q}, \tag{1.49}$$

which obey the SU(3) commutation relations

$$\left[\hat{G}_a^{(q)}, \hat{G}_b^{(q)}\right] = i f_{abc} \hat{G}_c^{(q)}. \tag{1.50}$$

1.2.2 Local non-Abelian Symmetry

Local SU(2) transformation is given by

$$\hat{\psi}^{(\frac{1}{2})\prime}(x) = \exp[ig\boldsymbol{\tau} \cdot \boldsymbol{\alpha}(x)/2] \hat{\psi}^{(\frac{1}{2})}(x). \tag{1.51}$$

In analogy with the U(1) case, the covariant derivatives in the SU(2) case is (cf. (1.26))

$$D^\mu \hat{\psi}^{(\frac{1}{2})} = (\partial^\mu + ig\boldsymbol{\tau} \cdot \boldsymbol{W}^\mu(x)/2)\, \hat{\psi}^{(\frac{1}{2})}, \tag{1.52}$$

with satisfying

$$D^\mu \hat{\psi}^{(\frac{1}{2})} \rightarrow D'^\mu \hat{\psi}^{(\frac{1}{2})\prime}(x) = \exp(ig\boldsymbol{\tau} \cdot \boldsymbol{\alpha}(x)/2) D^\mu \hat{\psi}^{(\frac{1}{2})}, \tag{1.53}$$

where $\boldsymbol{W}$ are three gauge fields in order to conserve this form under this local SU(2) transformations. Under local SU(2) transformations, $\boldsymbol{W}$ must transform as

$$\delta \boldsymbol{W}^\mu = \partial^\mu \boldsymbol{\epsilon}(x) - g[\boldsymbol{\epsilon}(x) \times \boldsymbol{W}^\mu] \tag{1.54}$$

in the infinitesimal case($\boldsymbol{\alpha} \rightarrow \boldsymbol{\epsilon}$).

1.3 Lagrangian for Gauge Fields

Invariance under local symmetries tell us how introduce the gauge field into the matter field. However, we have not known how the gauge field itself move yet. In this section, we start from the familiar theory, that is, Maxwell's theory, and generalize it to the SU(2) or SU(3) gauge fields.

1.3.1 Abelian Case

The Lagrangian

$$\mathcal{L}_A = -\frac{1}{4} F_{\mu\nu} F^{\mu\nu} \tag{1.55}$$

leads to the classical Maxwell's equations:

$$\Box A^\nu - \partial^\nu (\partial_\mu A^\mu) = 0, \tag{1.56}$$

where $F_{\mu\nu}$ is defined by

$$F_{\mu\nu} = \partial_\mu A_\nu - \partial_\nu A_\mu \tag{1.57}$$

and called *the field strength tensor*. This is the fundamental equation of QED, and expands to SU(2) weak theory, and SU(3) strong theory. Quantization of this is difficult because of the appearance of the unphysical state. Here, I do not state this argument in order to avoid the confusing. Instead we prepare for the generalization to SU(2) and SU(3). The relation (1.57) can be also derived from

$$[D^\mu, D^\nu]\psi \equiv (D^\mu D^\nu - D^\nu D^\mu)\psi = ieF^{\mu\nu}\psi. \tag{1.58}$$

If you know the method on the curved space, this can be understood by considering the infinitesimal translations in a closed loop, and $F^{\mu\nu}$ is related to the curvature in the curved space.

1.3.2 Non-Abelian Case

(1.58) is generalized to the SU(2) case:

$$[D^\mu, D^\nu]\psi^{(\frac{1}{2})} = ig\boldsymbol{\tau}/2 \cdot (\partial^\mu \boldsymbol{W}^\nu - \partial^\nu \boldsymbol{W}^\mu - g\boldsymbol{W}^\mu \times \boldsymbol{W}^\nu)\psi^{(\frac{1}{2})}, \tag{1.59}$$

where D^μ is given by (1.52). In the SU(2) case, the commutators of the covariant derivatives are

$$[D^\mu, D^\nu]\psi^{(\frac{1}{2})} = ig\boldsymbol{\tau}/2 \cdot (\partial^\mu \boldsymbol{W}^\nu - \partial^\nu \boldsymbol{W}^\mu - g\boldsymbol{W}^\mu \times \boldsymbol{W}^\nu)\psi^{(\frac{1}{2})}, \tag{1.60}$$

hence,

$$\boldsymbol{F}^{\mu\nu} = (\partial^\mu \boldsymbol{W}^\nu - \partial^\nu \boldsymbol{W}^\mu - g\boldsymbol{W}^\mu \times \boldsymbol{W}^\nu). \tag{1.61}$$

As expected, the Lagrangian describing the gauge fields is

$$\hat{\mathcal{L}}_{SU(2)} = -\frac{1}{4}\hat{\boldsymbol{F}}_{\mu\nu} \cdot \hat{\boldsymbol{F}}^{\mu\nu}. \tag{1.62}$$

Similarly, in the SU(3) case, we can follow the same procedure.

Note that all gauge fields do not have the explicit mass term, which spoils the gauge invariance. The gauge bosons are still massless. However, in the real world, some of the gauge bosons have their non-zero mass ($W^\pm$ and Z^0).

1.4 Spontaneously Symmetry Breaking

1.4.1 The Goldstone Model

If the vacuum is not unique in the system, spontaneously symmetry breaking becomes an important idea. We often require that the vacuum is invariant under the Lorentz

transformations and parallel translations. Due to this, the vacuum expectation value (VEV) of a scalar field can be non-zero:

$$\langle 0|\phi(x)|0\rangle = c \neq 0. \tag{1.63}$$

In contrast, any spinor field $\psi(x)$ and vector field V^μ can not have non-zero VEVs:

$$\langle 0\,|\,\psi(x)\,|\,0\rangle = \langle 0\,|\,V^\mu\,|\,0\rangle = 0. \tag{1.64}$$

In order to explain the idea of spontaneously symmetry breaking, we first consider the Goldstone Model. The Lagrangian is

$$\mathcal{L} = (\partial^\mu\phi^*(x))(\partial_\mu\phi(x)) - \mu^2|\phi(x)|^2 - \lambda|\phi(x)|^4, \tag{1.65}$$

with

$$\phi(x) = \frac{1}{\sqrt{2}}(\phi_1(x) + i\phi_2(x)) \tag{1.66}$$

being a complex scalar field, μ^2 and λ being real parameters. Note that the field is classical now, not quantized. (1.65) is invariant under the global U(1) phase transformations

$$\phi(x)\to\phi'(x) = e^{-i\alpha}\phi(x), \quad \phi^*(x)\to\phi^{*\prime}(x) = e^{i\alpha}\phi(x). \tag{1.67}$$

The Hamiltonian density corresponding to (1.65) is

$$\mathcal{H}(x) = (\partial^0\phi^*(x))(\partial_0\phi(x)) + (\boldsymbol{\nabla}\phi^*(x))\cdot(\boldsymbol{\nabla}\phi(x)) + \mathcal{V}(\phi), \tag{1.68}$$

where

$$\mathcal{V}(\phi) = \mu^2|\phi(x)|^2 + \lambda|\phi(x)|^4 \tag{1.69}$$

is the potential energy. If $\lambda < 0$, the potential is negative infinity at $\phi(x)\to\infty$, so take $\lambda > 0$ here. The minimum value of the Hamiltonian is determined by the $\mathcal{V}$ when $\phi(x)$ is constant. In this case, two situations occur (Figure 1.1):

1. $\mu^2 > 0$ case. In this situation, $\mathcal{V}(\phi)$ is positive definite. $\mathcal{V}(\phi)$ has the unique minimum value when $\phi(x) = 0$.

2. $\mu^2 < 0$ case. The minima is given by

$$\phi(x) = \phi_0 = \left(\frac{-\mu^2}{2\lambda}\right)^{1/2}\exp(i\theta), \quad 0 \leq \theta < 2\pi, \tag{1.70}$$

   and the vacuum is not unique any more.

   Due to the invariance of the Lagrangian, the value of θ is not significant. we take $\theta = 0$, so that

$$\phi_0 = \left(\frac{-\mu^2}{2\lambda}\right)^{1/2} = \frac{1}{\sqrt{2}}v \quad (>0) \tag{1.71}$$

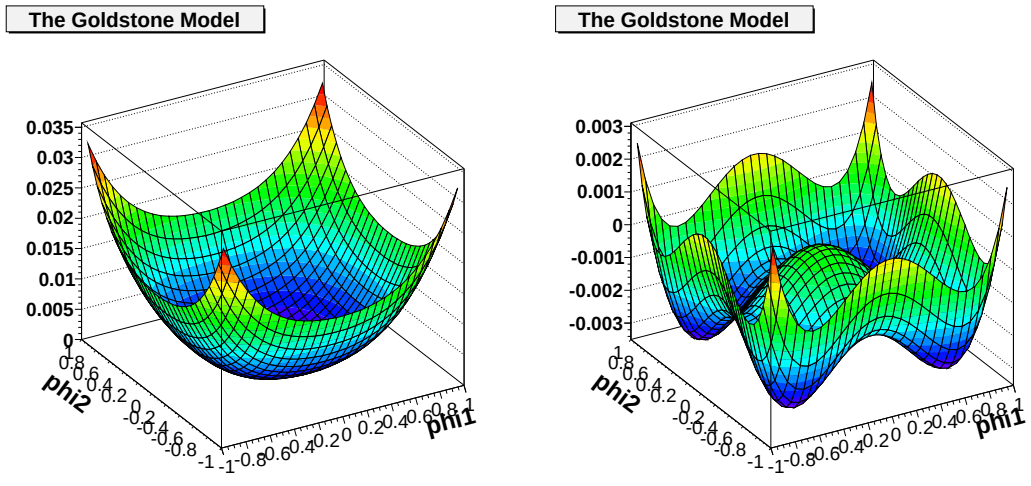

Figure 1.1: Spontaneous symmetry breaking in the Goldstone model. The left plot shows $\mu^2 > 0$ case and the right does $\mu^2 < 0$.

is real. We usually (or exaggeratingly always) treat the perturbative calculations using Feynman diagrams. If we proceed the second case straightforwardly, we cannot get the correct answer because $\phi = 0$ is unstable and we cannot treat the quartic term as the perturbative any more. Alternatively, we introduce two real fields $\sigma(x)$ and $\eta(x)$ which satisfies

$$\phi(x) = \frac{1}{\sqrt{2}}[v + \sigma(x) + i\eta(x)]. \tag{1.72}$$

We can interpret the two fields as the deviations from the new ground state. And by means of these, we can treat the Lagrangian perturbatively. Due to this, we can rewrite the original Lagrangian in terms of the new two fields so that

$$\begin{aligned}\mathcal{L} = \frac{1}{2}[\partial^\mu\sigma(x)][\partial_\mu\sigma(x)] - \frac{1}{2}(2\lambda v^2)\sigma^2(x) + \frac{1}{2}[\partial^\mu\eta(x)][\partial_\mu\eta(x)] \\ -\lambda v\sigma(x)[\sigma^2(x) + \eta^2(x)] - \frac{1}{4}\lambda[\sigma^2(x) + \eta^2(x)]^2\end{aligned} \tag{1.73}$$

where we have omitted the constant term. Note that the original Lagrangian and the rewritten one describes the same physics. However, the latter can be used as perturbative in contrast to the former can not.

We can interpret eq. (1.73) as the free part

$$\mathcal{L}_0 = \frac{1}{2}[\partial^\mu\sigma(x)][\partial_\mu\sigma(x)] - \frac{1}{2}(2\lambda v^2)\sigma^2(x) + \frac{1}{2}[\partial^\mu\eta(x)][\partial_\mu\eta(x)] \tag{1.74}$$

and the interaction part. The definition of vacuum is that no particles in this state, and therefore, from (1.71)

$$\langle 0\,|\,\phi(x)\,|\,0\rangle = \phi_0. \tag{1.75}$$

This is the condition for spontaneously symmetry breaking.

Note that the free Lagrangian (1.74) has two scalar fields: σ has the mass ($\sqrt{2\lambda v^2}$) and the other, η are massless field. Such a massless boson appears in spontaneously symmetry breaking theories always, and is called *Goldstone boson(s)*. Goldstone bosons are not observed in nature, so we can not accept the Goldstone model. Alternatively, we can proceed the Higgs Mechanism introduced in the next.

1.4.2 The Higgs Model

In the previous section, we start from global U(1) symmetry. Here, however, introduce the covariant derivatives

$$D_\mu\phi(x) = [\partial_\mu + iqA_\mu(x)]\phi(x) \tag{1.76}$$

instead of the ordinal derivatives, and add free gauge field Lagrangian

$$-\frac{1}{4}F_{\mu\nu}(x)F^{\mu\nu}(x). \tag{1.77}$$

Then these lead to the local invariant U(1) Lagrangian

$$\mathcal{L}(x) = [D^\mu\phi(x)]^*[D_\mu\phi(x)] - \mu^2|\phi(x)|^2 - \lambda|\phi(x)|^4 - \frac{1}{4}F_{\mu\nu}(x)F^{\mu\nu}(x), \tag{1.78}$$

which defines the *Higgs model*. This Lagrangian is invariant under the transformations

$$\phi(x) \;\rightarrow\; \phi'(x) = \phi(x)e^{-iqf(x)} \tag{1.79}$$

$$\phi^*(x) \;\rightarrow\; \phi^*(x) = \phi^*(x)e^{iqf(x)} \tag{1.80}$$

$$A_\mu(x) \;\rightarrow\; A'_\mu(x) = A_\mu(x) + \partial_\mu f(x). \tag{1.81}$$

As the Goldstone model, we assume that $\lambda > 0$ and two situations occur. In $\mu^2 > 0$ case, the vacuum is unique and the spontaneously symmetry breaking can not occur. For $\mu^2 < 0$, the vacuum is not unique. We can take the vacuum state as the Goldstone model (1.71) without loss of generality, and by introducing the real fields $\sigma(x)$ and $\phi(x)$ as defined by (1.72) the original Lagrangian (1.78) becomes

$$\begin{aligned}\mathcal{L}(x) = \frac{1}{2}[\partial^\mu\sigma(x)][\partial_\mu\sigma(x)] - \frac{1}{2}(2\lambda v^2)\sigma^2(x) - \frac{1}{4}F_{\mu\nu}(x)F^{\mu\nu}(x) + \frac{1}{2}(qv)^2A_\mu(x)A^\mu(x)\\ +qvA^\mu(x)\partial_\mu\eta(x) + \text{'interaction terms'},\end{aligned} \tag{1.82}$$

where the 'interaction terms' consist of the cubic or quartic terms. Eq. (1.82) is almost the same as the Goldstone model, but note that the fifth term of (1.82) couples the different fields. Therefore, this Lagrangian is not described in terms of the normal coordinates and we can not identify the A^μ and η fields as the massive vector boson and

the massless scalar boson respectively. This Lagrangian in terms of the "bad" coordinates can be rewritten in normal coordinates by the use of the gauge transformations (1.81), which transforms the complex field $\phi(x)$ to the real fields,

$$\phi(x) = \frac{1}{\sqrt{2}}[v + \sigma(x)], \tag{1.83}$$

and then the massless field η has disappeared. This gauge condition is known as the *unitary gauge*. The Lagrangian now becomes

$$\mathcal{L} = \mathcal{L}_0 + \mathcal{L}_I \tag{1.84}$$

where the free Lagrangian $\mathcal{L}_0$ is

$$\mathcal{L}_0(x) = \frac{1}{2}[\partial^\mu \sigma(x)][\partial_\mu \sigma(x)] - \frac{1}{2}(2\lambda v^2)\sigma^2(x) - \frac{1}{4}F_{\mu\nu}(x)F^{\mu\nu}(x) + \frac{1}{2}(qv)^2 A_\mu(x)A^\mu(x) \tag{1.85}$$

and the interaction terms are

$$\mathcal{L}_I(x) = -\lambda v\sigma^3(x) - \frac{1}{4}\lambda\sigma^4(x) + \frac{1}{2}q^2 A_\mu(x)A^\mu(x)[2v\sigma(x) + \sigma^2(x)]. \tag{1.86}$$

We eventually get the remarkable result, that is, starting from one *complex* scalar field and one *massless* vector field leads to one *real* scalar field and one *massive* vector boson. This is the *Higgs model* and the unphysical massless field η has been *eaten* by the gauge field via the gauge transformations.

1.5 Experimental Higgs Boson Mass Constraints

1.5.1 The Electroweak Precision Measurements

The electroweak parameters, the vector boson and top quark mass and its width, forward-backward asymmetry, and so on, are precisely measured by various experiments (ALEPH, DELPHI, L3, OPAL, SLD, CDF, DØ and NuTeV) in the world. The precision electroweak results have the sensitivity to the masses of the top and the Higgs boson through radiative (loop) corrections as shown in Figure 1.2. The parameter indicating the relation of the W boson and the Z boson mass with weak mixing angle at one loop is,

$$\rho = \frac{M_W^2}{M_Z^2(1 - \sin^2\theta_W)} \equiv 1 + \Delta r, \tag{1.87}$$

and a radiative correction are written by,

$$\Delta r = \frac{3G_F}{8\pi^2\sqrt{2}}m_t^2 + \frac{\sqrt{2}G_F}{16\pi^2}M_W^2\left[\frac{11}{3}\ln\left(\frac{M_h^2}{M_W^2}\right) + \cdots\right] + \cdots, \tag{1.88}$$

which is quadratic in the top quark mass, while the dependence on the mass of the Higgs boson is only logarithmic, therefore the top quark mass, especially if large, is the dominant parameter in the correction to electroweak processes [10].

The electroweak precision measurements allow the constraint on the SM Higgs boson mass [11]. The Figure 1.3 shows the $\Delta\chi^2$ of the fit to all electroweak measurements as a function of SM Higgs Mass. From the fitting, the constraint SM Higgs mass with the experiment uncertainties are obtained as,

$$M_h = 84^{+34}_{-26}\ \mathrm{GeV}/c^2, \tag{1.89}$$

the shaded band represents the uncertainty due to uncalculated higher-order corrections. And the 95% one-sided confidence level upper limits on the SM Higgs mass is,

$$M_h < 154\ \mathrm{GeV}/c^2, \tag{1.90}$$

when the 95% confidence level lower limits on the SM Higgs mass 114.4 GeV/c^2 from direct searches as discussed in the following section is included, the upper limit increases to 185 GeV/c^2.

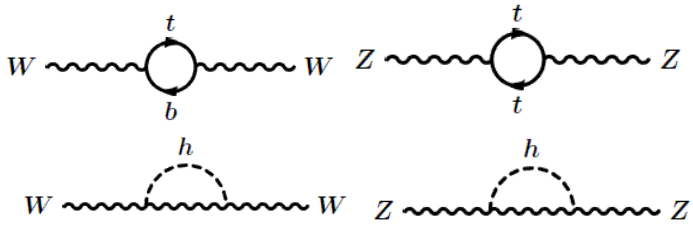

Figure 1.2: Radiative loop correction for electroweak processes.

1.5.2 The SM Higgs Boson Searches at LEP

The four LEP collaborations, ALEPH, DELPHI, L3, and OPAL set a lower bound of the SM Higgs bosons at 95% confidence level using the combined result [12]. The LEP collaborations have collected a total of 2461 pb^{-1} of e^+e^- collision data at $\sqrt{s} = 189 - 209$ GeV which are used to search for the SM Higgs boson. The four results are combined and examined in a likelihood test for their consistency with two hypotheses, the background hypothesis and the signal plus background hypothesis.

The SM Higgs boson is expected to be produced mainly in association with Z as $e^+e^- \to Zh$, and the SM Higgs boson is expected to decay mainly into $b\bar{b}$ pairs. The target final state are the 4-jets event ($Zh \to q\bar{q}b\bar{b}$), the missing energy event ($Zh \to \nu\bar{\nu}b\bar{b}$), the leptonic event ($Zh \to \ell^+\ell^-b\bar{b}$, $\ell = e, \mu$), and the tau lepton event ($Zh \to \tau^+\tau^-b\bar{b}$).

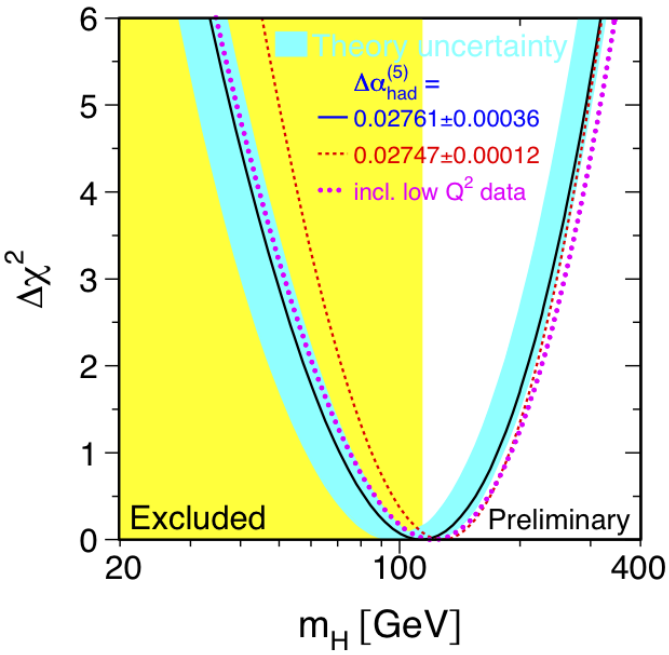

Figure 1.3: The $\Delta\chi^2$ of the fit to the electroweak precision data as a function of SM Higgs mass. The solid line results by including all data, and the blue band is the estimated theoretical error from missing higher-order corrections.

The ratio $CL_s = CL_{s+b}/CL_b$ is used to drive a lower bound on the SM Higgs boson mass, where CL_{s+b} means the compatibility for the observation and signal + background hypothesis, and CL_b is the compatibility for the observation and background hypothesis. Using The quantity for setting exclusion limits by taken a mass hypothesis into account to be excluded at the 95% confidence level if the corresponding value of CL_s is less than 0.05. The combined the final results from the four LEP experiments is a lower bound of 114.4 GeV/c^2 on the mass of the SM Higgs boson at the 95% confidence level as shown in Figure 1.4.

1.5.3 Higgs Boson Searches at Tevatron

In July 2010, CDF and DØ combined results are published [1]. We exclude $158 < m_H < 175$ GeV/c^2 high-mass region for the standard model Higgs boson by combining CDF/DØ analysis at the confidence level 95 %. This results is deduced by using integrated luminosities $\mathcal{L} = 5.9$ fb^{-1} in CDF and $\mathcal{L} = 6.7$ fb^{-1} in DØ. There, the Higgs boson decay modes studied are $H \to b\bar{b}$, $H \to W^+W^-$, $H \to \tau^+\tau^-$, and $H \to \gamma\gamma$.

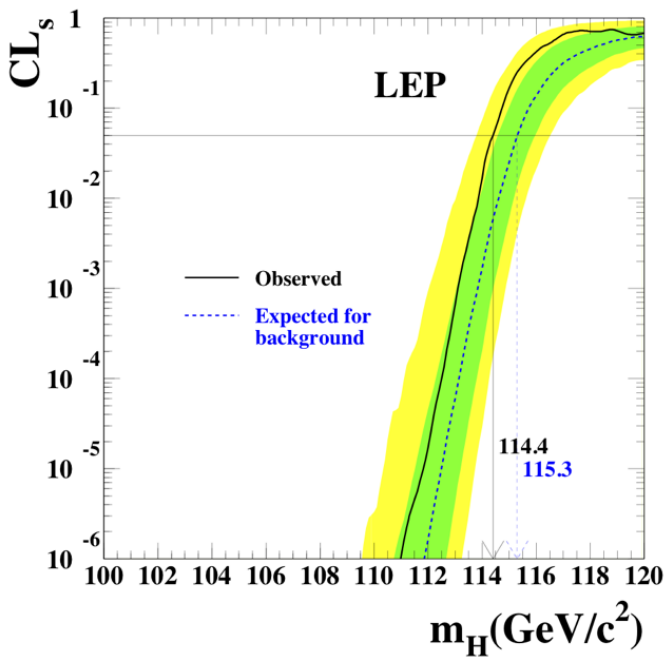

Figure 1.4: Confidence Level CL_s for the signal+background hypothesis in Higgs production at LEP2. The yellow green and yellow band around the median expected line correspond to the 68% and 95% probability bands, respectively.

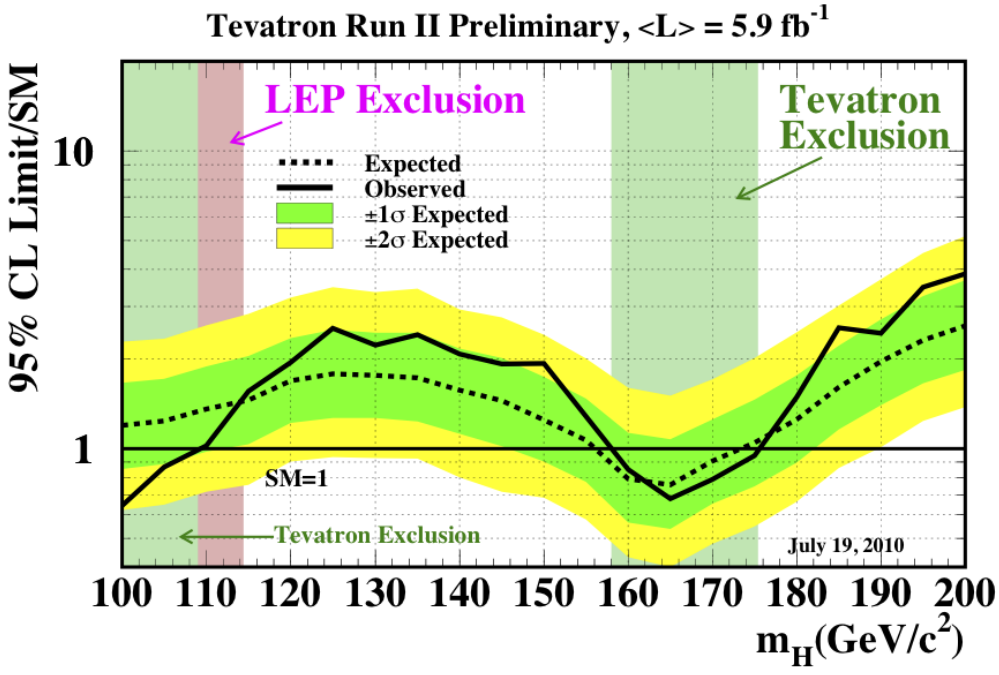

Figure 1.5: Standard Model Higgs Boson Limit. The details can be found in [1].

Chapter 2

Experimental Apparatus

The Tevatron Collider is the high energy frontier accelerator in particle physics. The Tevatron is located at Fermilab in Batavia, Illinois USA. It is currently providing highest energy proton-antiproton collisions with $\sqrt{s} = 1.96$ TeV. The collisions occur at two points in Tevatron ring which has a radius of about 1km. The collision points are instrumented with a detector in each which called The Collider Detector at Fermilab (CDF II) and DØ. This study uses data collected with the CDF II. The CDF II is a general purpose solenoidal detector which combines precision charged particle tracking, scintillator based calorimetry, and muon detection chambers and scintillators. This chapter describes the beam production and acceleration system, and the CDF II detector design.

2.1 The Accelerator Complex

The Tevatron is the last in a chain of accelerators that gradually increase the energy of protons and antiprotons. The protons are abundant and readily in nature, while antiprotons must be produced and stored. In addition, a single accelerator cannot bring particles from rest to very high energies because no magnets have the dynamic range necessary. Consideration of these requirements led to the design of a chain of accelerators at Fermilab. Figure 2.1 shows a diagram and aerial photograph of the Fermilab accelerator chain.

2.1.1 Proton Production and Boosting

The Cockcroft-Walton pre-accelerator provides the first stage of acceleration. The accelerator ionizes the hydrogen gas to H^+ ions, which are accelerated to 750 keV of kinetic energy.

The ionized hydrogen gases (H^+) enter a liner accelerator (Linac), approximately 150m long, and the ions are accelerated to 400 MeV. The acceleration in the Linac is done by a series of "kicks" from Radio Frequency (RF) cavities.

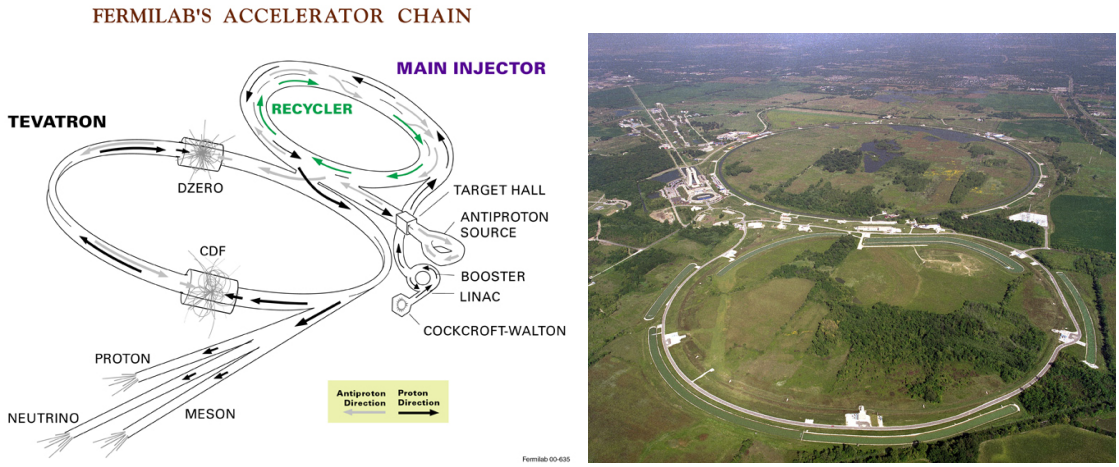

Figure 2.1: A diagram (left) and aerial photograph (right) of the Fermilab accelerator chain.

The H^+ ions with 400 MeV are injected into the Booster. The Booster is a circular synchrotron, approximately 150m in diameter. A carbon foil strips the electrons from the H^+ ions, leaving behind protons. The intensity of the protons beam is increased by injecting new protons into the same orbits as the circulating ones. The protons are accelerated from 400 MeV to 8 GeV with a series of magnets arranged around a 75m radius circle, with 18 RF cavities interspersed.

2.1.2 Main Injector

The Main Injector (MI) is a circular synchrotron seven times the circumference of the Booster and slightly more than half the circumference of the Tevatron. Main Injector has 18 accelerating cavities. It can accelerate 8 GeV protons from the Booster to either 120 GeV or 150 GeV, depending on their destination. When used to stack antiprotons, the final energy is 120 GeV. When used to inject into the Tevatron, the final beam energy is 150 GeV. As well as accepting protons from Booster, the Main Injector can accept antiprotons from the Antiproton Source. The Main Injector can accelerate beam as fast as every 2.2 seconds.

2.1.3 Antiproton Source

In order to produce antiprotons, the protons with 120 GeV are extracted from the MI and strike a nickel target at the Antiproton source. These high-energy protons striking the target produce a spray of all sorts of secondary particles. Using magnets to choose which momentum and charge we can collect 8 GeV antiprotons from this spray. Approximately one antiproton is produced per 10^5 protons. These antiprotons are directed into the Debuncher.

The Debuncher is a rounded triangular-shaped synchrotron with a mean radius of 90m. It can accept 8 GeV antiprotons from the target station, and maintain the beam at a energy of 8 GeV. Its primary purpose is to efficiently capture the high momentum spread antiprotons coming from the target using a RF manipulation called bunch rotation which reduce the antiproton momentum spread. The reduction is done to improve the Debuncher to Accumulator transfer because of the limited momentum aperture of the Accumulator at injection.

The Accumulator is also triangular-shaped synchrotron and is mounted in the same tunnel as the Debuncher. It is the storage ring for antiprotons, all of the antiprotons made are stored here at 8 GeV and cooled until need.

2.1.4 Recycler

The Recycler is an antiproton storage ring installed in the same tunnel as the MI. The proposed purpose of the Recycler was to recycle the antiproton from a Tevatron store, cooling them and storing them alongside those sent from the Antiproton Source. This was abandoned after early problems in RunII. The Recycler now accepts transfers only from the Antiproton Source and cools them further than the antiprotons Accumulator is capable. The Recycler uses both a stochastic cooling system and an electron cooling system. Stochastic cooling is used to cool the beam in Recycler, but loses its effectiveness with higher intensities. Once above 2×10^{12} antiprotons in the Recycler, Electron cooling is required. Electron cooling works on the principle of momentum transfer between electrons and antiprotons, a highly concentrated, cool beam of electrons is driven at the same energy as the antiprotons and laid overtop of the antiprotons. The resulting glancing collisions between electrons and antiprotons transfer some of the momentum from the "hot" antiprotons to the "cool" electrons. With enough electrons, a substantial longitudinal cooling force is produced by absorbing momenta from the antiprotons allowing for more compact, brighter bunches to send to the Tevatron.

2.1.5 Tevatron

The Tevatron is the largest of the Fermilab accelerators, with a circumference of approximately 6km long. It is a circular synchrotron with eight accelerating cavities. The Tevatron can accept both protons and antiprotons from MI and accelerate them from 150 GeV to 980 GeV. In Collider mode, the Tevatron can store beam for hours at a time. Because the Tevatron is a primarily storage ring, the length of time between acceleration cycles is widely variable. The Tevatron is the cryogenically cooled accelerator. The magnets used in the Tevatron are made up of a superconducting niobium/titanium alloy that needs to be kept extremely cold ($\sim$4 K) to remain a superconductor. The benefit of having superconducting magnets is the increased magnetic fields possible when high currents can be run through thin wires without fear of damage related to excessive resistive heating.

2.1.6 Luminosity

The luminosity of collisions can be expressed as:

$$\mathcal{L} = \frac{f N_B N_p N_{\bar{p}}}{2\pi(\sigma_p^2 + \sigma_{\bar{p}}^2)} F\left(\frac{\sigma_l}{\beta^*}\right), \tag{2.1}$$

where f is the revolution frequency, N_B is the number of bunched, $N_{p(\bar{p})}$ is the number of protons (antiprotons) per bunch, and $\sigma_{p(\bar{p})}$ is the protrons (antiprotons) RMS beam size at the interaction point. F is a form factor which corrects for the bunch shape and depends on the ratio of σ_l, the bunch length to β^*, the beta function, at the interaction point. The beta function is a measure of the beam width, and it is proportional to the beam's x and y extent in phase space. Table 2.1 shows the accelerator parameter in the current run (Run II). The current peak luminosity is $\sim 3.6 \times 10^{32}$ cm^{-2}s^{-1}. The delivered luminosity is 5.4 fb^{-1} and actual recorded luminosity is 4.5 fb^{-1}, which is collected between February 2002 and December 2008. Figure 2.2 shows integrated luminosity measured with CDF.

Parameter	Run II
Number of bunhes (N_B)	36
Bunch length [m]	0.37
Bunch spacing [ns]	396
Protons/bunch (N_p)	2.7×10^{11}
Antiprotons/bunch ($N_{\bar{p}}$)	3.0×10^{10}
Total antiprotons	1.1×10^{12}
β^* [cm]	35
Interactions/crossing	2.3

Table 2.1: Accelerator parameters for Run II configurations.

2.2 The Collider Detector at Fermilab

The CDF II detector [13] is a general purpose solenoidal detector which combines precision charged particle tracking with fast projective calorimetry and fine grained muon detection. Figure 2.3 and Figure 2.4 show a cut away view and elevation view of the CDFII detector for each. Tracking systems are made up Silicon Trackers, Central Outer Tracker (COT), and Superconducting Solenoid which to measure precise trajectories and momenta of charged particles and reconstruct vertices. The solenoid surround the Silicon Trackers and COT, has 1.5m in radius and 4.8m long, and generates a 1.4 T magnetic field parallel to the beam axis. Calorimetry Systems measure the energy of particles, surround the solenoid. Muon Chambers detect the particles penetrating both Tracking Systems and Calorimetry Systems. Muons deposit small amount of ionization

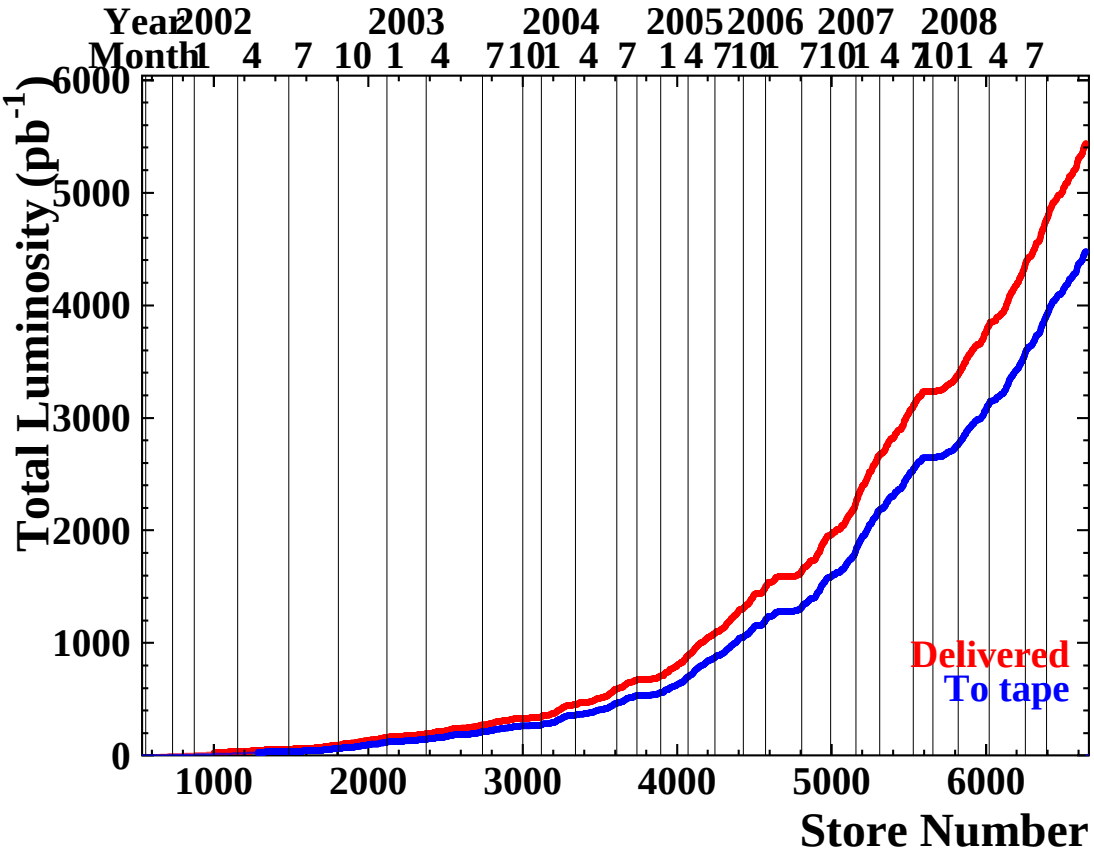

Figure 2.2: Integrated luminosity as a function of store number between February 2002 and December 2008.

energy in the material because they act as minimally ionizing particles (MIP), that is, the penetrating particles are mostly muons.

2.3 Coordinate System in the CDF

The standard coordinate system to be used in the CDF is the right-handed coordinate system. The z-axis is oriented the direction of the proton beam. The x-axis points horizontally away from the detector and the y-axis is vertical pointing up-wards. It is helpful to use the cylindrical coordinate. The azimuthal angle ϕ is $x-y$ plane angle around the beam line. The polar angle θ is measured starting from the z-axis. The rapidity of a particle is defined as,

$$y \equiv \frac{1}{2}\ln\left(\frac{E+p_z}{E-p_z}\right). \tag{2.2}$$

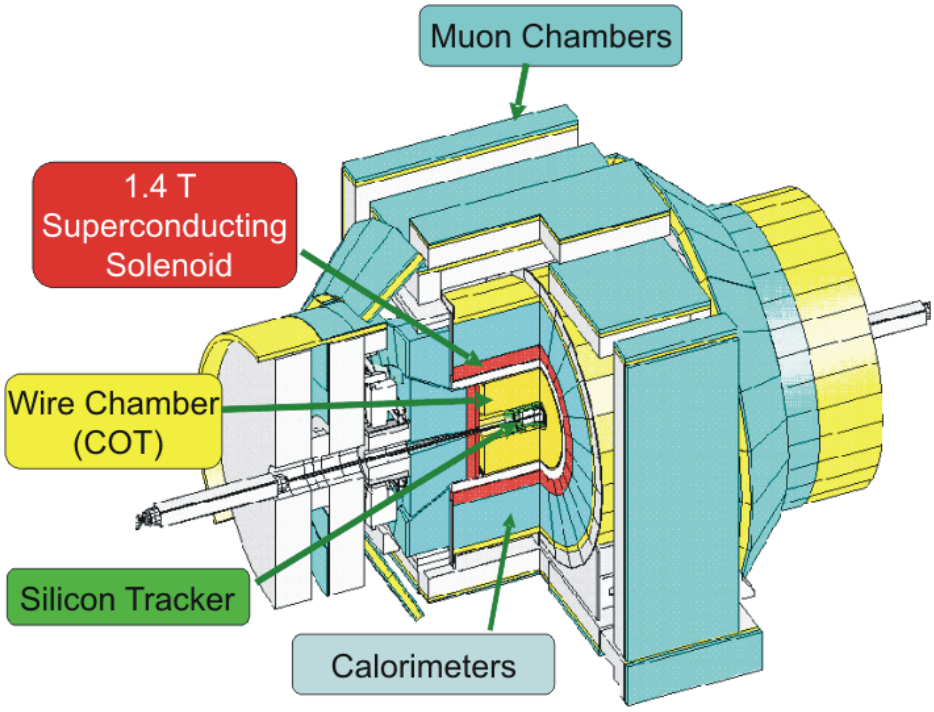

Figure 2.3: Cut away view of the CDF II detector.

where E is the energy of the particle and p_z is its longitudinal momentum. For highly boosted particles, $E \sim p$ and $p_z = p\cos\theta$, that is, the rapidity can be approximated by pseudorapidity,

$$\eta = -\ln\left(\tan\frac{\theta}{2}\right). \tag{2.3}$$

2.4 Tracking Systems

For CDF analysis technique, precision charged particle tracking is very important. CDF II detector has an open cell drift chamber, the Central Outer Tracker (COT) covers the region $|\eta| \leq 1.0$. Inside the COT, a silicon "inner tracker" is built from three components. Layer 00 (L00) is mounted on the beam pipe, very close to the beam line. Its primary purpose is to improve the impact parameter resolution. A micro-vertex detector at very small radii, so-called Silicon Vertex Detector (SVX-II), establishes the ultimate impact parameter resolution. Two additional silicon layers at intermediate radii, so-called Intermediate Silicon Layers (ISL), provides p_T resolution and b-tagging in the forward region $1.0 \leq |\eta| \leq 2.0$, and stand-alone silicon tracking over the full region $|\eta| \leq 2.0$. The stand-alone silicon segments allow integrated tracking algorithms which maximize tracking performance over the whole region $\eta \leq 2.0$. In the central region ($\eta \leq 1.0$), the stand-alone silicon segment can be linked to the fill

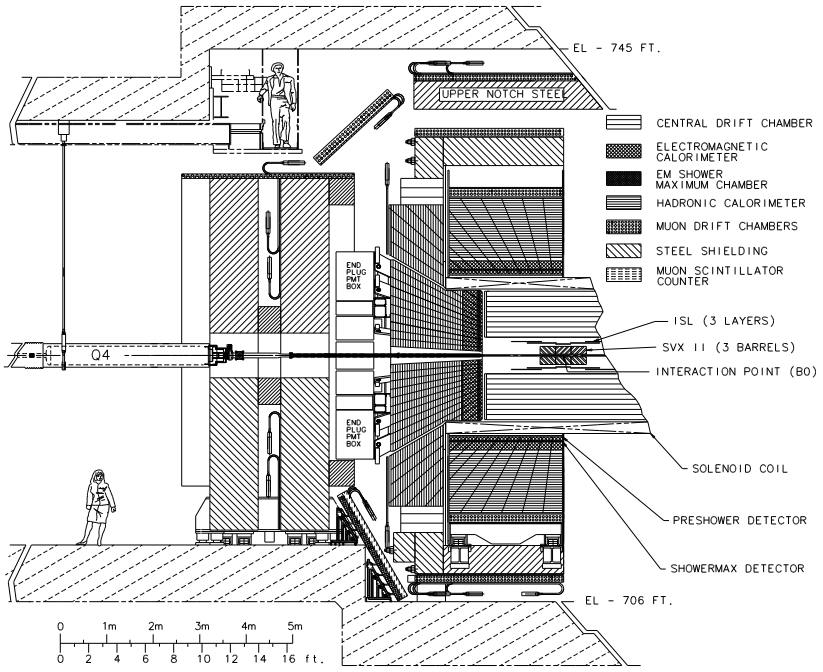

Figure 2.4: Elevation view of the CDF II detector.

COT track to give excellent p_T and impact parameter resolution.

2.4.1 Layer 00

Layer 00 [14, 15] is installed directly in the beam pipe. L00 was added at beginning of RunII for two reasons. Firstly to improve the impact parameter resolution of the CDF detector. Placement of a minimal material silicon layer at a smaller radius provides a precise measurement. Secondly, L00 was installed to extend the useful lifetime of the silicon system. The inner layers SVX-II will have a limited lifetime due to radiation damage. The design has six narrow (128 channels) and six wide (256 channels) groups in θ at $r = 1.35$cm and $r = 1.62$cm respectively. There are six readout modules in z, with two sensors bounded together in each module for a total length of 95cm. The sensors are single-sided p-in-n silicon with a 25(50)μm implant(readout) pitch. These have been produced by Hamamatsu Photonics (HPK), SGS-Thompson (ST) and Micron. These sensors can be biased up to 500V, limited by the maximum range of the power supplies. Figure 2.5 shows the end view of L00 and a part of SVX-II (L0 and L1).

2.4.2 Silicon Vertex Detector

Silicon Vertex Detector (SVX, SVX-II) [16] is the core detector for silicon tracking and for a trigger on tracks with large impact parameter with respect to the interaction

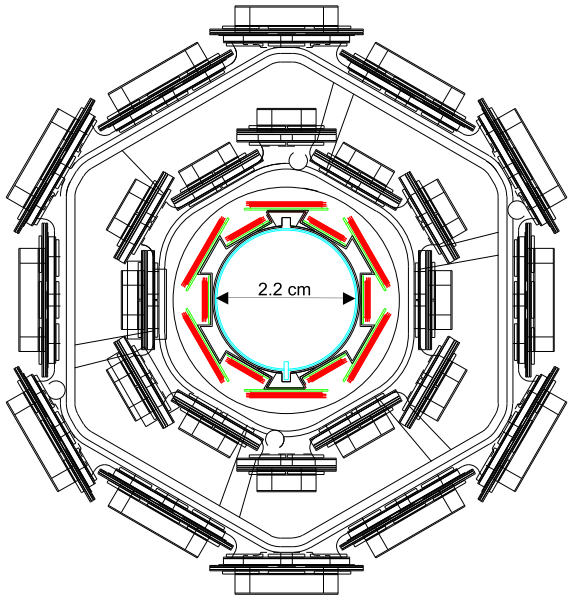

Figure 2.5: End view of Layer 00 (colored), also showing a part of SVX-II (un-colored).

point [17]. The SVX-II detector has 5 layers of double-sided sensors surround the L00 at radii from 2.5 to 10.6cm. Three layers (L0, L1, and L3) are made of Hamamatsu silicon with the n strips perpendicular to the p strips. The remaining two layers (L2 and L4) are Micron sensors with a stereo angle of 1.2° between the n and p strips. The strip pitch varies between 60 to 140μm, depending on the layer radius. The maximum bias voltages that can be applied to Hamamatsu and Micron sensors are 170 V and 70 V respectively, limited by the breakdown voltage of the integrated coupling capacitors and subtle sensor effects. The SVX-II can provide track information to $|\eta| < 2.0$. Table 2.2 shows the design parameters of the SVX-II. Figure 2.6 shows 3D view and $r - \phi$ view for SVX-II.

2.4.3 Intermediate Silicon Layers

Intermediate Silicon Layers (ISL) [18, 19] provides an extended forward coverage and links tracks between the COT and The SVX-II, and also can provide stand-alone 3D track information in the forward region. The ISL detector has one central layer at radius of 22cm covering $|\eta| < 1.0$, and two forward layers at radii of 22cm and 28cm covering $1 < |\eta| < 2$, with total length of 3m. It is made of double-sided silicon with strips at a stereo angle of 1.2°, and a strip of 112μm. The breakdown voltage of the sensors is 100V limited by the breakdown voltage of the coupling capacitors.

Parameter	Layer 0 (L0)	Layer 1 (L1)	Layer 2 (L2)	Layer 3 (L3)	Layer 4 (L4)
Number of ϕ strips	256	384	640	768	896
Number of z strips	512	576	640	512	896
stereo angle (degree)	90	90	+1.2	90	−1.2
ϕ strip pitch [μm]	60	62	60	60	65
z strip pitch [μm]	141	125.5	60	141	65
Total width [mm]	171.140	25.594	40.300	47.860	60.170
Total length [mm]	74.3	74.3	74.3	74.3	74.3
Active width [mm]	15.300	23.746	38.340	46.020	58.175
Active length [mm]	72.43	72.43	72.38	72.43	72.38
Number of sensors	144	144	144	144	144

Table 2.2: Design parameters of the Silicon Vertex Detector.

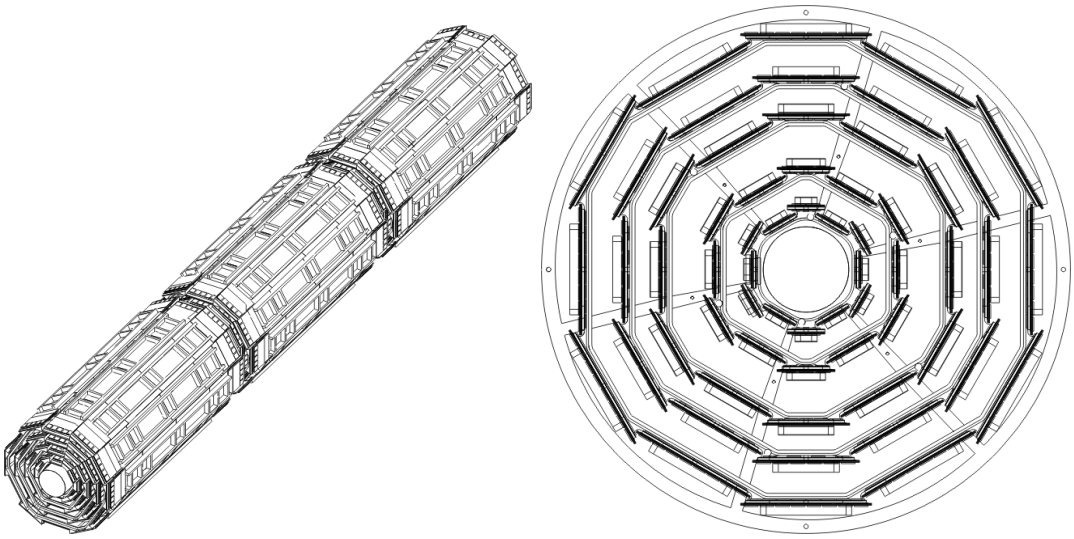

Figure 2.6: 3D view of the three barrels (left) and $r-\phi$ view of the barrel showing the 12 wedges with the 5 layers.

2.4.4 Central Outer Tracker

The Central Outer Tracker (COT) [20] is a cylindrical open-cell drift chamber spanning from 44 to 132cm in radii, and 310cm long. It operates inside a 1.4 Tesla solenoidal magnetic field and is designed to find charged tracks in the region $|\eta| \leq 1.0$. The hit position resolution is approximately 140μm and the momentum resolution $\sigma(p_T) = 0.0015\ (\mathrm{GeV}/c)^{-1}$. The COT is segmented into 8 super-layers alternating stereo and axial, with a stereo angle of $\pm 2^\circ$. Each super-layer contains 12 sense wires alternated with 13 potential wires which provide the field shaping within the cell yielding a total

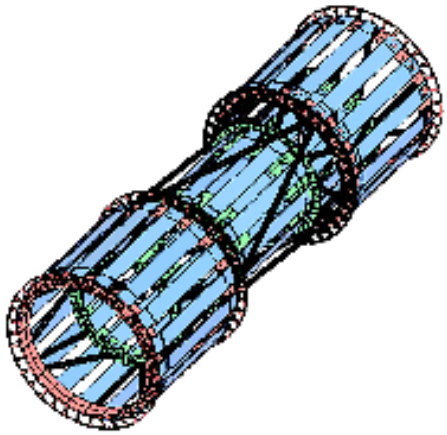

Figure 2.7: 3D veiw of the ISL spaceframe.

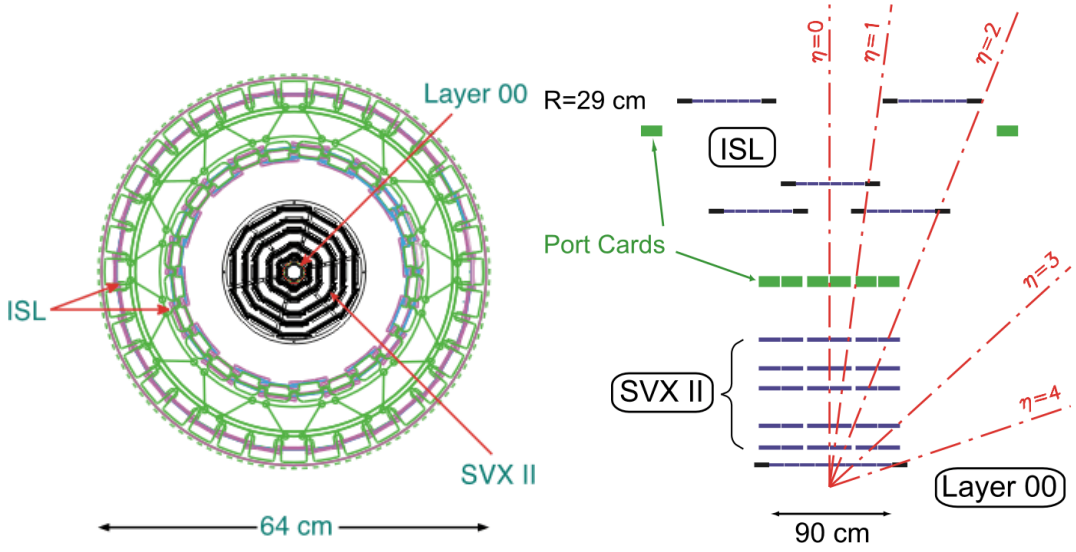

Figure 2.8: $r-\phi$ veiw (left) and $r-z$ view (right) of the silicon detectors.

of 96 measurement layers. For the entire cell chamber, there are 30,240 sense wires and 32,760 potential wires. Operating with an Argon-Ethane (50:50) gas mixture the maximum drift time is approximately 180 ns. The cells ate tilted at 35° to account for the Lorentz angle such that the drift direction is azimuthal. Tracks originating from the interaction point which have $|\eta| < 1$ pass through all 8 superlayers of the COT. Tracks which have $|\eta| < 1.3$ pass through 4 or more superlayers. Table 2.3 shows a mechanical summary of the COT. Figure 2.9 shows cell layout for super-layer 2 (SL2). Figure 2.10 shows the east endplate slots sense and field planes.

Parameter	
Gas (Argon:Ethane)	(50:50)
Number of Layers	96
Number of Super-layers	8
Stereo Angle (degree)	+2, 0, −2, 0, +2, 0, −2, 0
Cells/Layers	168, 192, 240, 288, 336, 384, 432, 480
Sense Wires/Cell	12, 12, 12, 12, 12, 12, 12, 12
Radius at Center of SL (cm)	46, 58, 70, 82, 94, 106, 117, 129
Tilt Angle	35°
Material Thickness	1.6% X_0
Drift Field	1.9 kV/cm
Maximum Drift Distance	0.88 cm
Maximun Drift Time	177 ns
Number of Channels	30,240

Table 2.3: Design parameters of the Central Outer Tracker.

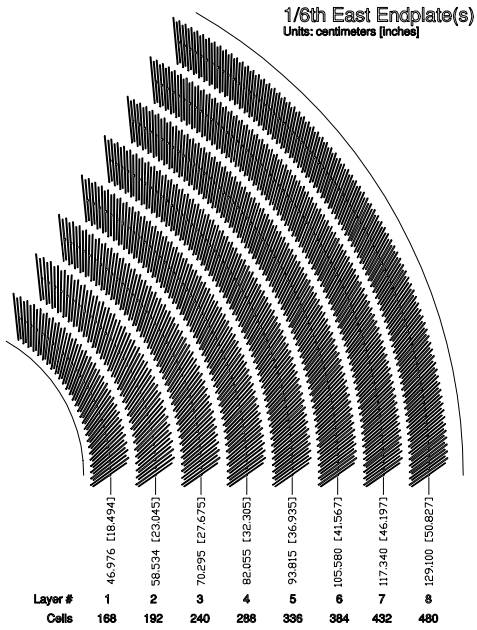

Figure 2.9: East endplate slots sense and field planes are at the clock-wise edge of each slot.

2.5 Calorimeter Systems

Segmented electromagnetic and hadron sampling calorimeters surround the tracking system and measure the energy flow of interacting particles in the $|\eta| < 3.6$. The

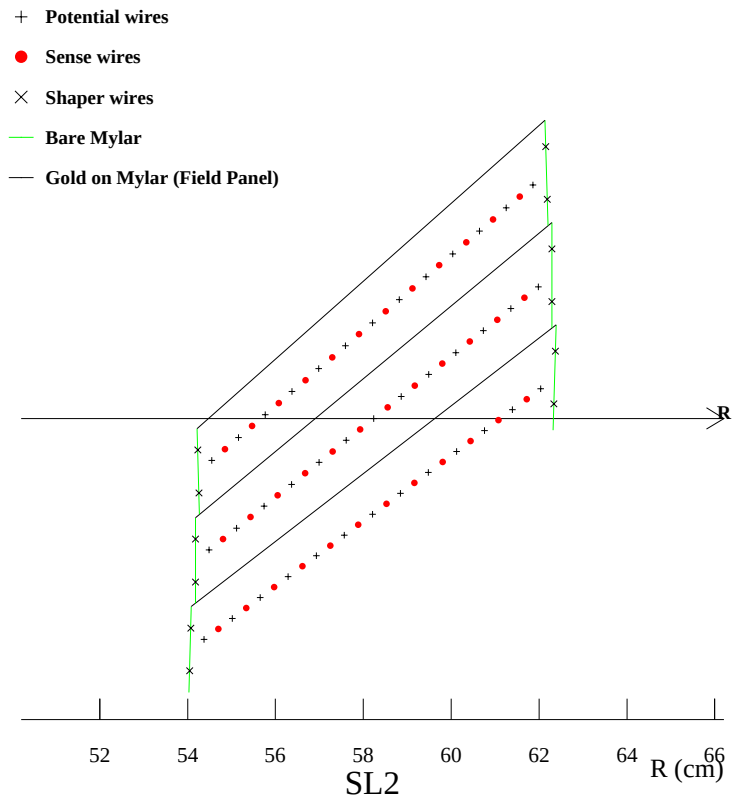

Figure 2.10: Nominal cell layout for SL2.

calorimeter systems are divided into 2 systems with respect to the pseudo-rapidity range, central and plug(forward) region. The Central Electromagnetic Calorimeter (CEM) covers the $|\eta| < 1.1$, which uses lead sheets interspersed with polystyrene scintillator as the active medium and employs phototube readout. The Central Hadronic Calorimeter (CHA) covers the $|\eta| < 0.9$, which uses steel absorber interspersed with acrylic scintillator as the active medium. The plug calorimeters, Plug Electromagnetic Calorimeter (PEM) and Plug hadron calorimeter (PHA), cover the $1.1 < |\eta| < 3.6$. They are sampling scintillator calorimeters which are read out with plastic fibers and phototubes.

2.5.1 Central Calorimeter

The Central Electromagnetic Calorimeter [21] detects electrons and photons and measures their energy. It is a lead-scintillator sampling system with tower segmentation, the each tower is 15° in $r - \phi$ plane. The CEM total thickness is 18 radiation length (32cm), to make sure that 99.7% of the electrons energy will be deposited. The CEM

energy resolution is

$$\frac{\sigma_E}{E} = \frac{13.5\%}{\sqrt{E_T}} \oplus 2\% \tag{2.4}$$

where E_T is the transverse energy in GeV, $\oplus$ symbol means that the constant term is added in quadrature to the resolution, and position resolution is typically 2mm for 50 GeV/c electrons.

The Central Electromagnetic Showermax Chamber (CES) is used to identify electrons and photons using the position measurement to match with tracks, the transverse shower profile to separate photon from π^0s, and pulse hight to help identify electromagnetic showers. The CES is located at approximately 6 radiation lengths deep at the expected shower maximum of particles in the EM calorimeter. The CES module is a multi-wire proportional chamber with 64 anode wires parallel to the beam axis.

The Central Preshower Detector (CPR) [22] is located at between the front face of the EM calorimeter and the magnet coil. The CPR can be useful in the $\pi-$photon separation and electron identification. The CPR was replaced the slow gas chamber with a faster scintillator version which has a better segmentation during RunII in 2004. The new CPR is used to improve the jet energy resolution.

The Central Hadronic Calorimeter [23] is an iron-scintillator sampling calorimeter, covering range $|\eta| < 0.9$, approximately 4.5 λ_0 interaction length, and the energy resolution is

$$\frac{\sigma_E}{E} = \frac{50.0\%}{\sqrt{E_T}} \oplus 3\%. \tag{2.5}$$

The Wall Hadronic Calorimeter (WHA) also an iron-scintillator sampling calorimeter, covering range $0.7 < |\eta| < 1.3$. The WHA is 4.5 λ_0 interaction length, and the energy resolution is

$$\frac{\sigma_E}{E} = \frac{75.0\%}{\sqrt{E_T}} \oplus 4\%. \tag{2.6}$$

2.5.2 Plug Calorimeter

The plug calorimeter covers $1.1 < |\eta| < 3.6$, corresponding to polar angles $3^\circ < \theta < 37^\circ$ as shown in Figure 2.11. Each plug wedge spans 15° in azimuth, however from $1.1 < |\eta| < 2.11$ (37° to 14°) the segmentation in ϕ is doubled, and each tower spans only 7.5°. There is an electromagnetic section (PEM) with a shower position detector (PES), followed by a hadronic section (PHA).

The PEM [24] is lead-scintillator sampling calorimeter, with unit layers composed of 4.5mm lead and 4mm scintillator. There are 23 layers in depth for a total thickness of about 21 X_0 radiation length at normal incidence. The PEM has an energy resolution is

$$\frac{\sigma_E}{E} = \frac{16\%}{\sqrt{E_T}} \oplus 1\%. \tag{2.7}$$

The PHA is an iron-scintillator sampling calorimeter, approximately 7 λ_0 in depth, and has an energy resolution of

$$\frac{\sigma_E}{E} = \frac{80\%}{\sqrt{E_T}} \oplus 5\%. \tag{2.8}$$

The PEM shower maximum detector is located about 6 λ_0 deep within the PEM, and is constructed of two layers of scintillating strips. The strips are 5mm wide, and roughly square in cross section. Position resolution of the PES is about 1mm. The summaries of design parameters for the calorimeter are shown in Table 2.4.

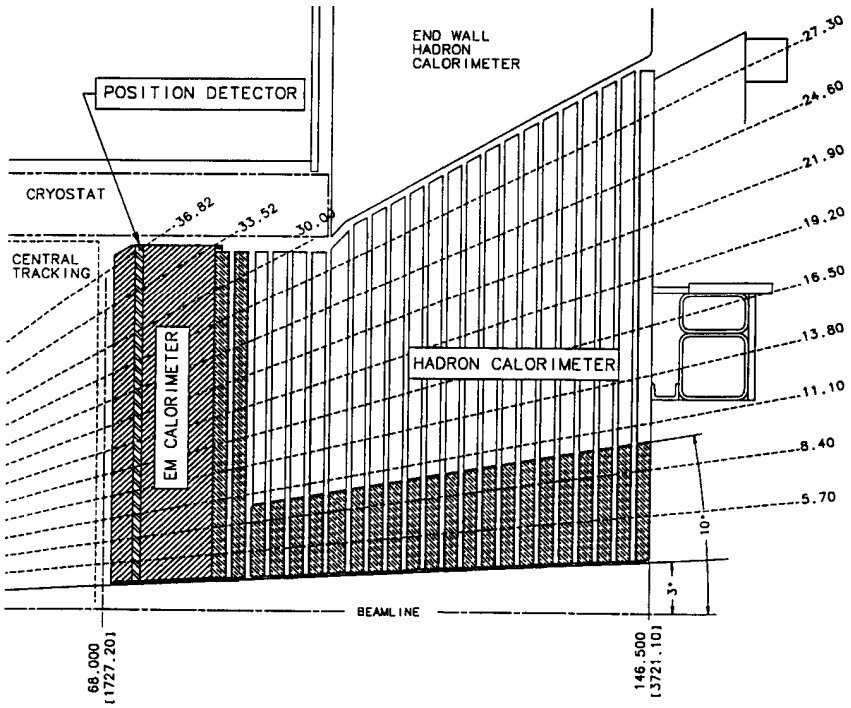

Figure 2.11: Cross section of the plug calorimeter (PEM and PHA).

2.6 Muon Detectors

Muons penetrate the tracking systems and the calorimeters leaving very little energy. The reason is muons produce much less bremsstrahlung than electrons and therefore do not produce electromagnetic showers, due to their larger mass. The CDF muon systems [13] use this property by placing detectors behind enough material. Muons deposit minimum ionizing energy in the calorimeters matched with a track in the

Calorimeter	Coverage	Energy Resolution (%)	Thickness	Absorber
CEM	$\|\eta\| < 1.1$	$13.5/\sqrt{E_T} \oplus 2$	18 X_0	3.18 mm lead
PEM	$1.1 < \|\eta\| < 3.6$	$16.0/\sqrt{E_T} \oplus 1$	21 X_0	4.5 mm lead
CHA	$\|\eta\| < 0.9$	$50.0/\sqrt{E_T} \oplus 3$	4.5 λ	2.5 cm iron
WHA	$0.7 < \|\eta\| < 1.3$	$75.0/\sqrt{E_T} \oplus 4$	4.5 λ	5.0 cm iron
PHA	$1.3 < \|\eta\| < 3.6$	$80.0/\sqrt{E_T} \oplus 5$	7.0 λ	5.08 cm iron

Table 2.4: Design parameters of the calorimeter.

COT. The momentum of these muons is measured by their bend in the solenoidal field using the COT. The central muon system is capable of detecting with transverse momentum $p_T \geq 1.4$ GeV, through their interaction with the gas and subsequent drift on the produced electrons toward the anode wires. The muon detectors consist of four separate subsystems: the central muon chambers (CMU), the central upgrade (CMP), the central muon extension (CMX), and the barrel muon detector (BMU). Table 2.5 shows design parameters of the muon detector. Figure 2.12 shows the effective muon detector coverage in $\eta - \phi$ plane.

The CMU detector locates directly outside of the central hadron calorimeter, 35 m from the interaction point, and covers the region of $|\eta| \leq 0.6$. It is divided into 24 east and 24 west 15° wedges. Each wedge contains three muon chambers and each muon chamber consists of four layers of four rectangular drift cells staggered in order to eliminate hit position ambiguities. A stainless steel sense wire a diameter of 50μm is located in the center of each cell. A muon object is created by forming a "stub" from hits in the muon chambers matching it to an extrapolated COT tracks.

The CMP consists of a second set of muon chambers behind additional 60cm of steel in the region $55° \leq \phi \leq 90°$. The chambers are fixed length in z and form box around the central detector. The pseudorapidity coverage thus varies with azimuth as shown in Figure 2.12.

The central extension consist of conical section of drift tubes (CMX) in polar angle from 42° to 55° ($0.6 \leq |\eta| \leq 1.0$). The top two wedges (Wedge 5 and 6) of the west CMX is called the "Keystone". There are no top 2 wedge on the east CMX due to cryogenic utilities servicing the solenoid. The bottom 6 wedges (Wedge 15-20) are called "Miniskirt". The design parameters of the muon detector are shown in Table 2.5.

2.7 Luminosity Monitor

The beam luminosity has been measured using the process of inelastic $p\bar{p}$ scattering. The cross section is $\sigma_{\rm in} \sim 60$ mb. The rate of inelastic $p\bar{p}$ interaction is given by

$$\mu f_{\rm BC} = \sigma_{\rm in} L \tag{2.9}$$

Muon detector	CMU	CMP	CMX
Coverage	$\|\eta\| < 0.6$	$\|\eta\| < 0.6$	$0.6 < \|\eta\| < 1.0$
Drift tube length [cm]	226	640	180
Max drift time [μs]	0.8	1.4	1.4
Total drift tubes	2304	1076	2208
Pion interation length (λ)	5.5	7.8	6.2
Minimum detectable muon p_T (GeV/c)	1.4	2.2	1.4

Table 2.5: Design parameters of the moun detector.

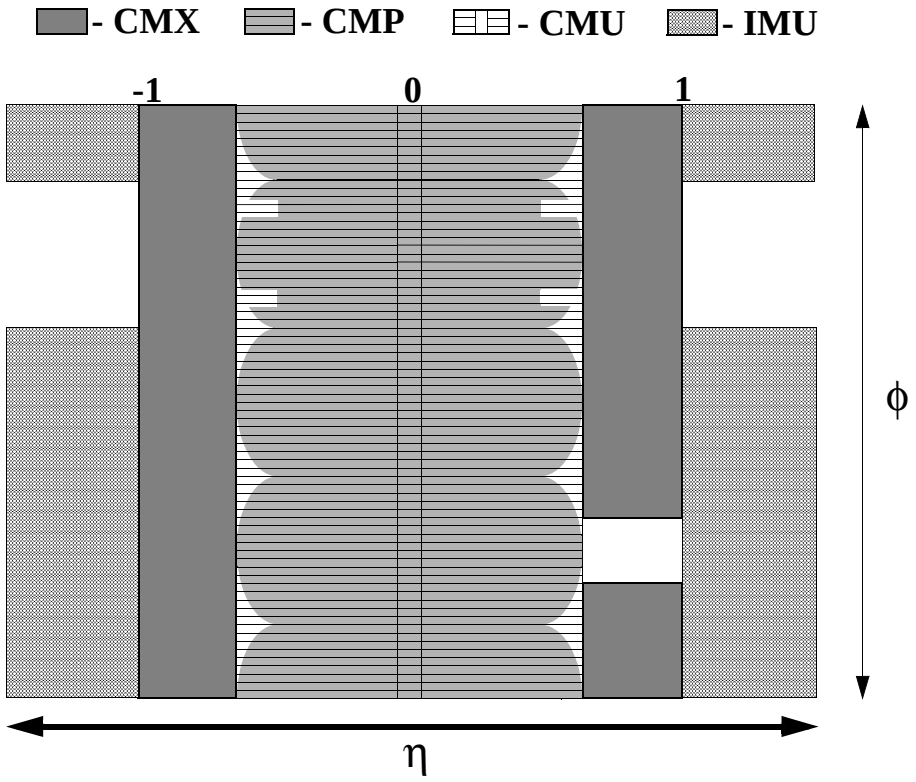

Figure 2.12: Muon detector coverage in $\eta - \phi$ plane.

where L is the instantaneous luminosity, $f_{\rm BC}$ is the rate of bunch crossing in the Tevatron and μ is the average number of $p\bar{p}$ interaction per bunch crossing. In CDF Run II, Cherenkov luminosity counters (CLC) [25, 26] is used to measure the luminosity by counting number of $p\bar{p}$ interaction μ accurately.

The detector consists of two modules which are located in the "3 degree holes" inside the end-plug calorimeter in the forward and backward region and which cover $3.7 < |\eta| < 4.7$ range. Each CLC detector module consists of 48 thin, long, conical,

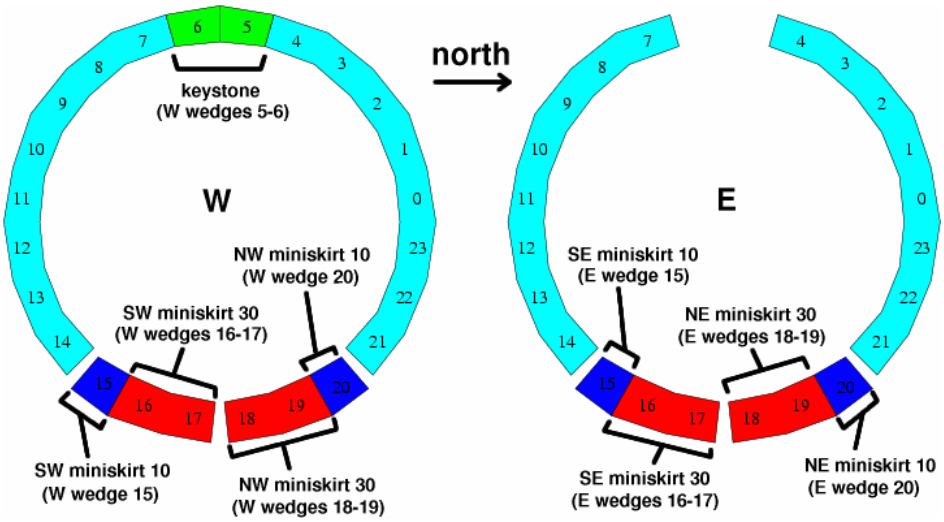

Figure 2.13: CMX detector in $r - \phi$ plane.

gas-filled Cherenkov counters. The counters arranged around the beam pipe in three concentric layers, with 16 counters each, and pointing to the center of the interaction region. They are built with reflective aluminized mylar sheets of 0.1mm thick and have a conical shape. The cones in two outer layers are about 180cm long and the inner layer counters have the length of 110cm. The Cherenkov light is detected with fast, 2.5cm diameter, photomultiplier tubes. The tubes have a concave-convex, 1mm thick, quartz window for efficient collection of the ultra-violet part of Cherenkov spectra and operate at a gain of 2×10^5. The counters are mounted inside a thin pressure vessel made of aluminum and filled with isobutane. The systematic uncertainty of the luminosity measurement is dominantly coming from the uncertainty of the inelastic $p\bar{p}$ cross section ($\sim 3\%$), the CLC acceptance ($\sim 2\%$), and the non-lineality of the CLC acceptance due to CLC occupancy saturates as growing luminosity due to the finite number of counters ($< 2\%$).

2.8 Trigger Systems

The trigger plays an important role on hadron collider experiment because the collision rate is much higher than the rate as which data can be stored on tape. The crossing rate of the Tevatron under 36 on 36 bunch operation is 7.6MHz, corresponding to 396 ns collision separation. The role of the trigger is to effectively extract the most interesting physics events from the large number of minimum bias events. For Run II, CDF employs a three-level trigger system to selectively capture interesting events. The levels are denoted simply as "L1", "L2" and "L3", with each subsequent level making more complicated decisions and requiring successively longer processing times. Figure 2.14 shows schematic of the CDF trigger system.

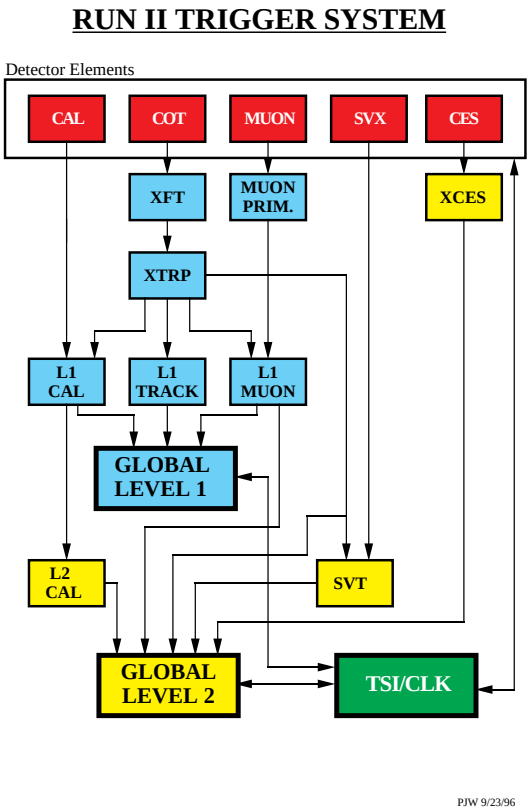

Figure 2.14: Book diagram of the trigger pass for Level 1 and Level 2.

2.8.1 Level-1

The first level of trigger selection Level-1 (L1) uses custom designed hardware to find physics objects based on a subset of the detector information and then makes a decision based on simple counting of these objects. The input to the L1 hardware comes from the calorimeters, tracking chambers and muon detectors. The decision to retain an event for further processing is based on the number and energies of the electron, jet and muon candidates as well as the missing energy in the event, or on the kinematic properties of few of these objects. The L1 hardware consists of three parallel synchronous processing streams which feed inputs of the single Global Level-1 decision unit. One stream finds calorimeter objects, another finds muons and the third finds tracks in the central region. The L1 trigger can be formed using these streams singularly as well as AND or OR combinations of them. All elements of the L1 trigger are synchronized to the same 132ns clock, with a decision made every 132ns by Global L1. In the period of the data taking considered in this analysis the accelerator was the two intermediate clock cycles automatically rejected. The maximum L1 accept rate is 20kHz, while the typical one is 12kHz.

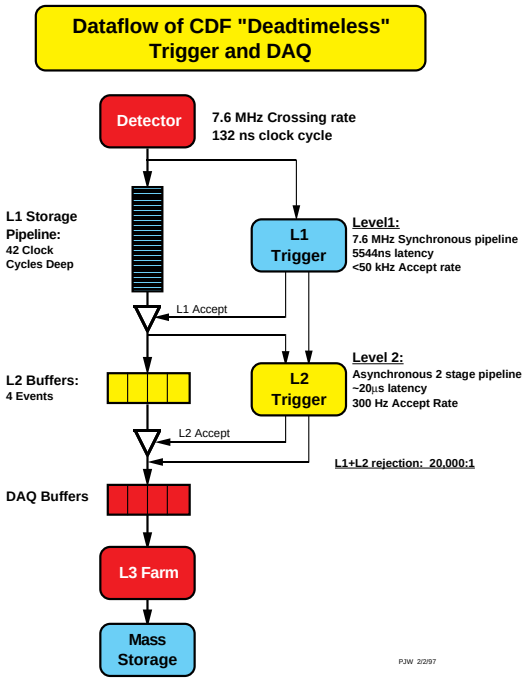

Figure 2.15: Schamatic diagram of the trigger and DAQ.

2.8.2 Level-2

Events accepted by L1 are processed by the second level of trigger Level-2 (L2), which is composed of several asynchronous subsystems. These provide input data to programmable L2 processors on the Global L2 crate, which determine if any of the L2 trigger are satisfied. Processing for L2 trigger decision starts after the event written into one of the four L2 buffers by a L1 accept. When L2 is analyzing the event in one of the buffers, that buffer cannot be used additional L1 accept. If all the four are full, the deadtime of the data acquisition is increased. It follows that the time required for a L2 decision needs to be less than about 80% of the average time between L1 accepts in order to keep the deadtime as low as possible. For this purpose L2 has been pipelined into two stages each taking approximately 10μs, which is sufficient to keep the deadtime at a minimum, even if L1 had an accept-rate of 50kHz. The L2 buffers perform a limited event reconstruction using essentially all the information used in L1, but with higher precision. In addition, at L2, data from the central shower-max detector and the SVX are available, which improve respectively the identification of electrons and photons and the reconstruction of the secondary vertices. Furthermore, a jet reconstruction algorithm is provided by the L2 cluster finder. After all of the data are stored in the processors, the event is examined to check if the criteria of any of the L2 triggers have been satisfied. This operation can be performed while the new events are being loaded into memory, thus not affecting the dead time. The typical L2 accept rate, as of this writing, is between 100 and 300Hz, depending on the initial luminosity.

2.8.3 Level-3

The Level-3 (L3) trigger subsystem is composed of two main components, the Event Builder (EVB) and the Level-3 Farm. Level-1 and Level-2 systems need to make their decisions at very high rate which makes it impossible to fully reconstruct each event. While Level-1 and Level-2 algorithms use small predefined pieces of event data to make their decision, the event pieces are stored in the buffers of the 140 Front End crates which constitute the EVB. After a L2 decision is made, the Event Builder assembles all event fragments from the Front End crates into one data block.

The 16 subfarms which compose the L3 Farm receive event fragments from the EVB and build complete events into the appropriate data structure for analysis. Since it takes about one second for one computer unit to make a trigger decision on one event, it takes a large farm of 250 Dual Pentiun Linux personal 5computers (called "processors") to ensure the required input rate. Each subfarm contains between 14 and 18 processor nodes and one "converter" node, which acts as "farm input" distributing the data flow coming from the EVB.

The events are then passed to a trigger algorithm (a different one for each processor) that categorizes the event and makes the decision as to whether or not to permanently store it. The selected event are passed to the Data Logger subsystem. During the building processing, the event integrity is checked. The L3 algorithms take advantage of the full detector information and improved resolution unavailable to lower trigger levels. This includes full three-dimensional track reconstruction and tight matching of tracks to calorimeter and muon-system information. Results from the lower level are used or drive the algorithms, which are based on the off-line analysis packages. This is a modular and separated filter modules for specific triggers. L3 accept events with a rate of approximately 75Hz.

Chapter 3

Monte Carlo Simulation

In order to understand data, we usually use Monte Carlo method to generate pseudo events. The data collected by the real collisions are complicated because of the following reasons:

1. the process is generated by the quarks and gluons inside of proton or antiproton, which could not measure directly in the data,

2. we have to analysis the signal and background at the same time. That is, we could not measure several components perfectly, especially coming from physics backgrounds.

For the real data, we analyze the following procedures:

1. run machine (here, Tevatron) to get events,

2. detect information for the final state particles by using detectors,

3. reconstruct events,

4. analyze the data.

In case of Monte Carlo simulations (virtual reality), the procedures are replaced by

1. run event generator to get events,

2. detect information for the final state particles by using detector simulations,

3. the same above,

4. the same above.

Once we get the Monte Carlo events, we can use them as the real data, and compare them to real ones.

3.1 Parton Distribution Functions

Both p and $\bar{p}$ are not point particles.They consists of the valence quarks and sea quarks, including antiquarks and gluons. We can interpret physics processes by using feynman diagrams, which is calculated perturbatively. (Strictly speaking, we can calculate the complicated paticle process, e.g. pion, by introducing the form factors, but this is not easy to estimate for p or $\bar{p}$.)

In order to interpret this composite system in terms of the elemental particles, we need to translate the information from p or $\bar{p}$ to the initially elemental particles. CTEQ [27], the Coordinated Theoretical-Experimental Project on QCD, provides the parton distribution functions (PDFs). PDFs are defined by the probability density for finding a particle with longitudinal momentum x at a given momentum transfer Q^2. We use CTEQ5L (L means the leading order) PDFs based on fixed target analysis, HERA's data and the Tevatron inclusive jet data (Figure 3.1).

3.2 Monte Carlo Event Generation

In high energy physics, there are some event generators, e.g. PYTHIA, ALPGEN, MadGraph/MadEvent, and so on. There are some character in each generator, but we use only PYTHIA to generate events in this analysis. Here we briefly give some explanation for each generators in which we are interested.

3.2.1 PYTHIA

PYTHIA is one of the most common event generator in CDF group. PYTHIA 8.1 written in C++ have already been released, but it does not cover PYTHIA 6.4 written in fortran 77 completely. Therefore, we use 6.4 for its stability.

This program also contains many routines, e.g. fragmentation/hadronization, parton showers, DIS and photon physics, beyond the SM physics, etc. The event generator in PYTHIA can handle simple Feynman diagrams. However, it does not take care of color and polarization effect well. When color and polarization effects are not significant, however, it performs very well.

3.2.2 MadGraph/MadEvent

MadGraph/MadEvent ([28], [29]) is a Monte Carlo generator that can calculate arbitrary tree-level diagrams with full colr and spin polarization information included. In this thesis, it is not used, but we want to embed standalone MadGraph for deducing the amplitudes for several processes to construct fully kinematical discriminant. This details are shown in Appendix A.

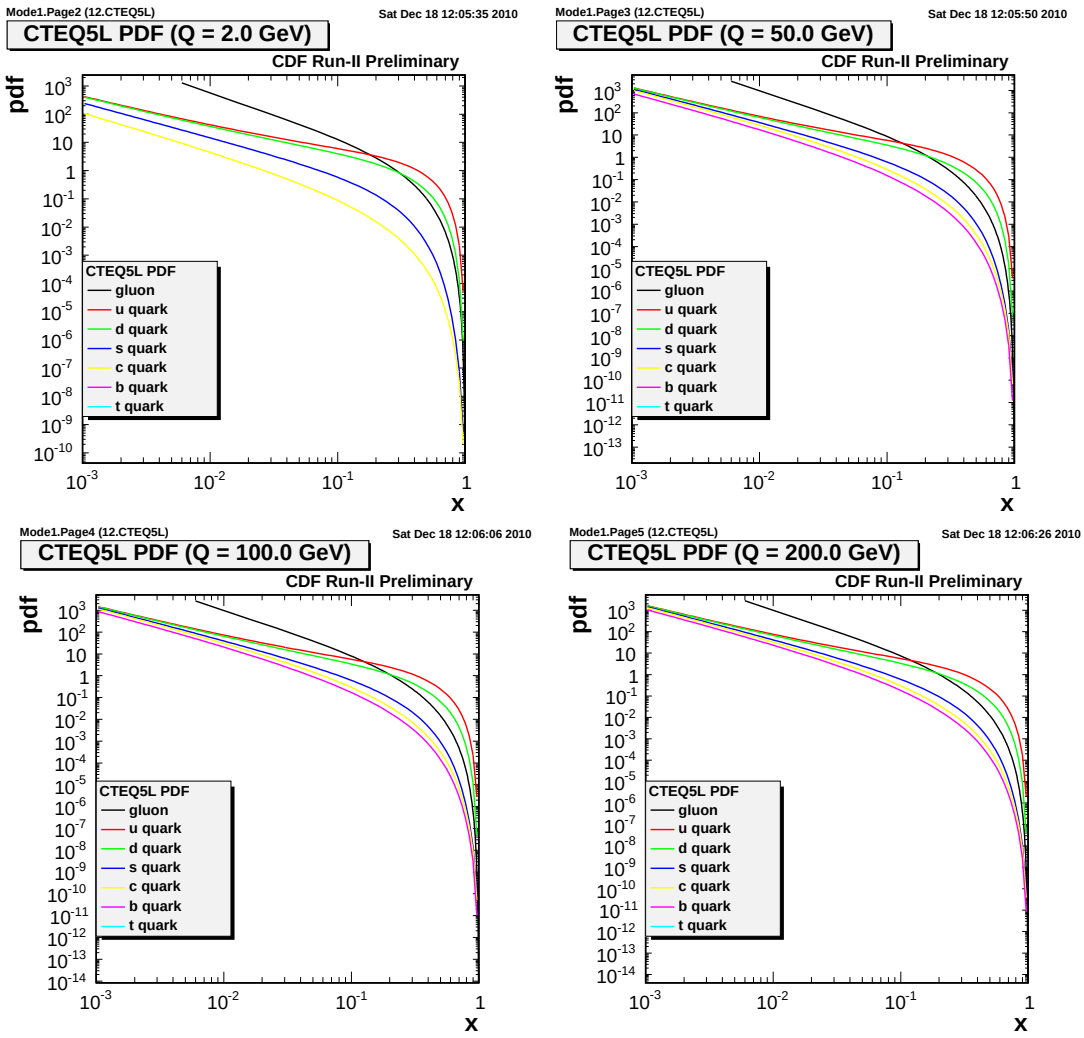

Figure 3.1: CTEQ5L PDFs. Anti-quark distributions are not shown in these plots.

3.3 Initial and Final State Radiation

In general, we can think that shower is composed of many branch of small pieces: $a \to b + c$, where a is called the mother and b and c the two daughters. The branches in PYTHIA are $q \to qg, g \to gg, g \to q\bar{q}, q \to q\gamma$ and $l \to l\gamma$. Photon branches, $\gamma \to q\bar{q}$ and $\gamma \to l\bar{l}$ are not included because of significantly rare events.

In PYTHIA, final state showers are well defined. However, initial state showers are not as sophisticated as the final state because they are not understood well theoretically compared to the final state. Still, the program works good for real data.

3.4 Beam Remnants and Underlying Events

If there are only hard processes, it was easy to analyze these events. In real life, however, various effects to analyze the hard process need to be considered.

First, a beam remnant, which does not include the parton initiating the hard process, affect to the final state particles. It is sometimes connected final state particles including final and initial state radiation by color confinement strings, and then form hadrons (Figure 3.2).

Second, p or $\bar{p}$ is not elementary but composite particle, so several pairs of partons in p or $\bar{p}$ can produce scatterings at the same time. It is called *"multiple interactions"* (Figure 3.3). This additional scattering can be hard, but the bulk of them should normally be soft compared to the primary interaction because of the infrared peaking of the cross section.

Third components affecting the hard process is *"pile-up"* events, which is similar to the multiple interactions. The difference between them is that the former is scattering for partons in another p or $\bar{p}$ interactions in the same bunch crossing due to high luminosity in contrast to partons in the same p or $\bar{p}$ for the latter (Figure 3.4).

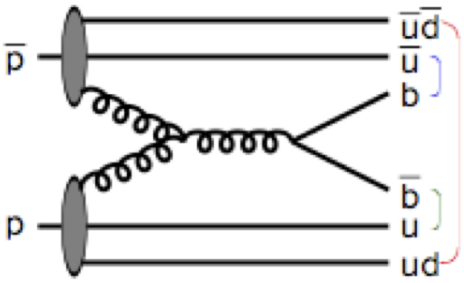

Figure 3.2: Beam Remnants with color connections.

3.5 Fragmentation/Hadronization

QCD perturbation theory is only valid at short distance for quarks and gluons. When they separate at long distance, QCD becomes strongly interacting and this perturbation theory breaks down. At our observation stage, the colored quarks and gluons are transformed into colorless hadrons, which process is called *hadronization* or *fragmentaion*. In the manual of PYTHIA [30], the term "hadronization" is used for the

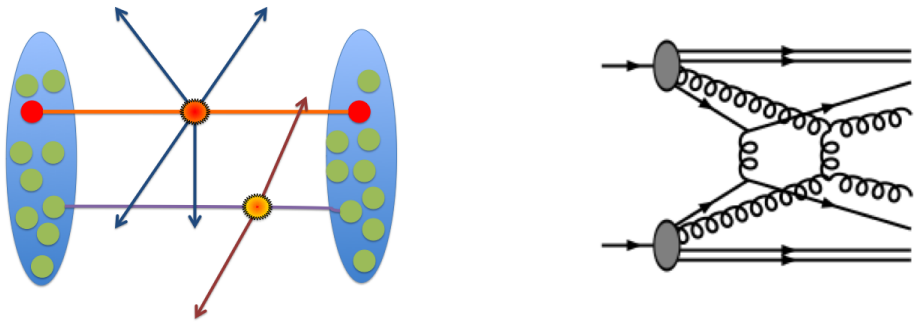

Figure 3.3: Multiple parton-parton interactions. The left illustration shows the hard prosess (red circles) with soft process (green circles) in p or $\bar{p}$ (blue circles). The right shows the same process in terms of Feynman diagram.

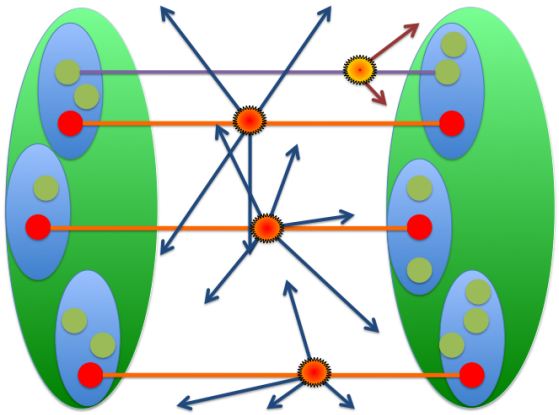

Figure 3.4: Pile-up events. The green circle shows one bunch.

combination of fragmentation and the subsequent decay of unstable particles, and we also adopt this convention in this thesis.

Once the distance between quarks is larger than about 1 fm, typical hadronic size, the potential is very large and generate quark-antiquark pair between them in order to connect the original quarks connect to the new quark/antiquark and reduce the distance (Figure 3.5).

3.6 Detector Simulation

Once the final long-lived particles have been generated by hadronizations, we have to consider the detectors how to react with these particles. This requires a full detector simulation which is composed of the various subdetector components, including

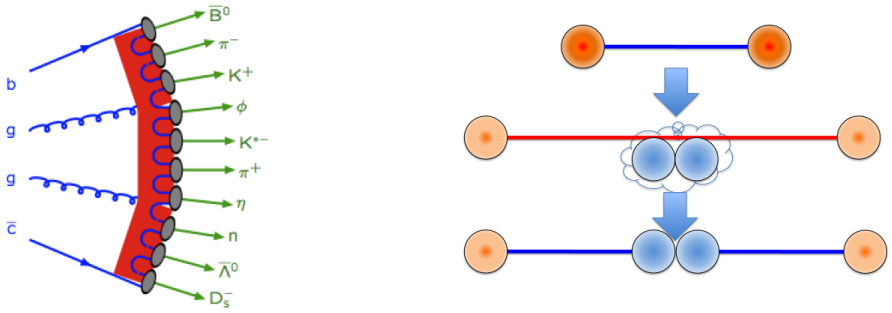

Figure 3.5: Hadronization process. The left illustrates the partons progress to colorless we observe. The right shows the simple illustration of apperance for new quark-antiquark pair between the original pair and separation in order to reduce the string potential.

resolution effects, inherent inefficiencies of the detector.

CDF uses a program called GEANT [31] to model the tracking in the volume of the detector.GEANT allows the construction of a mathematical model of the detector which can simulate the passage of charged particles through it, including showering to secondary or tertiary particles. This is used for the charge deposition models to simulate the response of the tracking detectors (silicon and COT).

Because modeling the interactions of each paricle and all its secondary particles takes a long time to simulate, CDF stops using GEANT after the first inelestic collision occurs in the calorimeter. Instead, it switches to a parameterized calorimeter response, tuned to test beam data, which employs a program called GFLASH [32]. This repidly and accurately simulates the response of the calorimeter towers to the energy deposited by the incoming charged particles, completing the detector simulation.

Chapter 4

Dataset and Event Selection

Proton-antiproton collisions produce many backgrounds compared to the signals of the Higgs boson even if the triggers reduce some backgrounds. Therefore, it is reasonable to add further cut for reducing backgrounds. In the early analysis, cut-based method was used for event selection. However, it is not adequate for the search for Higgs boson due to small (cross section) $\times$ (branching fraction). Previous analysis for the like-sign dilepton analysis showed that likelihood-based lepton identification has better performance than the cut-based method in the central region[33] and we expect that the method is useful for the plug objects.

4.1 Dataset and Triggers

Our dataset is collected by inclusive high-p_T lepton (electron and muon) trigger. However, in this thesis, we use MC events instead of data because of under studying these analysis, and not confirmed by CDF collaborators.

4.2 Event Selection

Although trigger requirements reduce some backgrounds, the data contains non-negligible backgrounds. In order to search for the Higgs boson, we require additional conditions to the events and/or leptons to improve the ratio of the signal to the background.

4.2.1 Pre-Event Selection

The pre-event selections are used in several studies and estimations described in this thesis. One is $|z_{\rm pv}|$, which is the location of the z-axis for the *"primary vertex"*. Primary vertex has the highest p_T-sum of associated tracks. This selection is applied to ensure well-defined measurement of collisions with the detector.

The other is the cosmic ray veto. Cosmic rays contaminate our interesting events coming from collisions by mimicking muons or electrons. This veto is achieved to look

at the direction of the trajectory and crossing timing by the fact that the cosmic rays are coming from outside of the detector, while the muon from collisions are from the center of the detector.

4.2.2 Central Electron Identification

The electron identification is achieved by using series of selection criteria, tracking and energy clustering, and the validated test beam. Central electron (CEM) are only desirable object in the region $|\eta| < 1.2$. The selections are categorized into 3 parts: *"geometrical and kinematical cuts"*, *"track quality cuts"*, and *"identification cuts (ID cuts)"*.

Geometrical and Kinematical Cuts

- Electron Fiducial:
  This variable ensures that the electron is reconstructed in a region of the detector which well instrumented. The electron position in the CEM is determined using either the value determined by the CES shower or by the extrapolated track, and it must satisfy the following requirements.
  - The electron must lie within 21cm of the tower center in the $r - \phi$ view in order for the shower to be fully contained in the active region $|z_{\rm CES}| < 21$cm.
  - The electron should not be in the regions $|z_{\rm CES}| < 9$cm, where the two halves of the central calorimeter meet, and $|z_{\rm CES}| > 230$cm, which corresponds to outer half of the last CEM tower. This region is prone to leakage into the hadronic part of the calorimeter.
  - The electron should not be in the region immediately closest to the point penetration of the cryogenic connections to the solenoidal magnet, which is uninstrumented. This corresponds to $0.77 < \eta < 1.0$, $75 < \phi < 90$ degree, and $|z_{\rm CES}| < 193$cm.
- High transverse energy (E_T):
  The transverse electromagnetic energy deposited by electron is calculated as the electromagnetic cluster energy multiplied by $\sin\theta$, where θ is the polar angle provided by the best COT track pointing to the EM cluster.
- High transverse momentum (p_T):
  The transverse momentum of the COT track as measured by using the track curvature in the COT.

Track Quality Cuts

- COT hits requirement:
  To ensure that the track associated with the electron or muon is good quality

reconstructed track, require that track has been reconstructed in the COT in 3 axial and 3 stereo superlayers with at least 7 hits in each.

- The relative position to primary vertex in z plane ($z_0 - z_{\rm pv}$):
  Separation between z coordinate of the closest approach point with respect to run average beam line (z_0) and primary vertex z position ($z_{\rm pv}$).

- Silicon hits requirement:
  The track is required hitting to some SVX layers (>3). The requirement critical plays to reject the residual photon conversion events which are considerable background in the LS dilepton events.

- Impact parameter (d_0):
  This variable is recalculated to take the x coordinate of the primary vertex. The cuts is the most powerfully for rejecting cosmic rays background.

Central Electron ID Variables

In the previous analysis, we choose 8 variables for the likelihood method. However in this thesis, the ID variables are used only for the 1st electron selection (cut-based method).

- E/p
  This is defined by the ratio of the cluster energy to the beam constrained COT track momentum. If the object pointing calorimeter cluster is an electron, its momentum measured by the COT track should match with the energy measured for the calorimeter cluster, i.e. $E/p \simeq 1$.

- χ^2_{strip}
  The pulse height shape in the strip view (r-z) of the CES detector is compared to the same profile extracted from test-beam data of electrons using χ^2 test. To allow for a comparison that is valid for energies lower than 10 GeV, the raw χ^2_{strip} is multipied by $(p/10.0)^{\alpha}$, where the p is the track momentum and α is given by

$$\alpha = 0.85 + 0.15\exp(-p/15.0) - p/1000\,. \tag{4.1}$$

- HA/EM
  This quantity is the ratio of 2-tower hadronic energy deposited in the CHA/WHA to the 2-tower electromagnetic energy deposited in the CEM. This ratio should be small, that is, the energy deposition in the electromagnetic calorimeter is much higher than that in the hadronic calorimeter.

- $L_{\rm shr}$
  The purpose of this quantity is to provide some discrimination of electrons and photons from hadronic showers faking these particles in the CEM. This is done

by comparing the observed energy sharing between towers to that expected for a true electromagnetic shower taken from test-beam data:

$$L_{\rm shr} = 0.14 \sum_i \frac{E_i^{\rm adj} - E_i^{\rm exp}}{\sqrt{(0.14\sqrt{E})^2 + (\Delta E_i^{\rm exp})^2}} \,, \tag{4.2}$$

where $E_i^{\rm adj}$ is the measured energy in towers adjacent to the seed tower, $E_i^{\rm exp}$ is the expected energy in the adjacent towers from test beam data, $\Delta E_i^{\rm exp}$ is the error on the energy estimate.

- $Q \times \Delta x_{\rm CES}$
  The $\Delta x_{\rm CES}$ is the distance, in units of cm, in the r-ϕ plane between the track extrapolated to the radius of the CES and the actual cluster position measured by the CES. We sign it with the charge of the candidate track.

- $\Delta z_{\rm CES}$
  This variable is the distance, in units of cm, in the r-z plane between the track extrapolated to the CES radius and the actual cluster position measured by the CES.

- $E_{\rm CES}/p^*$
  This is the ratio of the wire cluster pulse height measured in the CES, corrected for chamber warps, to the $p^* = 10(p/10)^\alpha$, where the p is the track momentum and α is defined in Eq. (4.1). The value for a real electron is expecteed to be around 1. The CES responses are sensitive to the shower development which is expected to be different between electrons and interactive pions.

- CPR or CP2
  The response of the CPR or CP2 detector corresponding to an electron cluster in units of the number of minimum-ionizing-particles (MIPs). The peak position corresponding to one MIP is identified by using muons. The CPR/CP2 responses are also sensitive to the shower-development as well as the CES responses.

4.2.3 Plug Electron Selection

For the 2nd electron, we apply the minimam cuts and LLID method for better signal efficiency. In this analysis, we reject standalone and phoenix electrons in the plug region because of many charge mismeasurements compared to outside-in electrons. However, outside-in electrons has considerable charge mismeasurements compared to the central region. Therefore, when we include the outside-in electrons to search for the Higgs boson, we must consider the rate of charege mismeasurements.

Geometrical and Kinematical Cuts

- Electron Fiducial
  - $|\eta|$
    This variable ensures the region that exists silicons and COT. We require $1.2 < |\eta| < 2.0$ for Outside-In electrons described below. $|\eta| < 2.0$ ensures this electron is passing in COT region, and $1.2 < |\eta|$ reject the poor calorimeter region.
  - Low transverse energy E_T
    The same as the central. We require plug electron has greater than 6 GeV.
  - Low transverse momentum p_T
    The same as the central. We require plug electron has greater than 6 GeV/c.

Track Quality Cuts

- Type
  - COT Outside-In Silicon
    requires a COT outside in track with non-zero number of both COT and silicon hits.
  - Phoenix
    requires a Phoenix track with ≥ 3 silicon $r-\phi$ hits, no stereo or z silicon hits. Chooses Phoenix track with minimum χ^2/d.o.f.
  - Standalone
    requires a max p_T track selected by CdfEmObject::maxPtTrack with zero COT hits and ≥ 3 silicon hits.
  - Anytrack
    takes one of the three track types above, trying in order COT Outside-In Silicon, Phoenix, Standalone.
- $N_{silicon}$
  For good electron requirement, we impose at least 3 hits. If only a few hits exist, tracking becomes ambiguous.

ID Variables

- χ^2_{PEM}
  The shower profile in the PEM detector is compared to the predicted Lorentz distribution and the χ^2 is calculated.

- E_5/E_9
  Clusters resulting from true electrons tend to have a narrow energy distribution. This can be seen in the PES shower maximum detector, where the energy of the five strips at the center of the cluster (E_5) is compared to the energy of all nine strips in the cluster (E_9) for both layers of the PES (U and V layer).

- $\Delta R_{PEM-PES}$
  The distance in the $x-y$ plane between the position of the reconstructed cluster in the PEM calorimeter and the PES shower maximum detector. This removes a background from poorly reconstructed clusters that might be a fake electron.

- E_{had}/E_{EM}
  This variable is the same as the central.

- PPR (Plug Preshower)
  This works as the same as the CPR/CPR2 for discriminating the electrons from jets by using the difference of the shower developments. This variable has not been used in the cut-based method.

4.2.4 Fake Lepton Candidates in the Jet Samples

For background PDF templates, we select jet samples (Jet 20, 50, 70, 100). We require some criterion to fake lepton candidates in jet samples. Leptons in jet sample is all fake leptons by definition.

We select fake leptons as the most same as electrons in the Monte Carlo signal samples. However, we impose additional requirement to leptons or events in the jet samples: W veto, Z veto, and away the second leading jet.

W veto

We do not want the real electron in jet sample, and we operate this by using Missing E_T and lepton energy. We reject the events which satisfy both criteria:

- electrons with $E_T > 20$ GeV or muons with $p_T > 6$ GeV/c passing lepton selection shown in Table 4.1.

- $\not\!\!E_T > 30$ GeV or transverse mass > 40GeV/c^2.

  Note that $\not\!\!E_T$ is corrected for muon passing our muon selection $p_T > 6$ GeV/c.

Z veto

We reject Z events by requiring

- electrons with $E_T > 20$ GeV or muons with $p_T > 20$ GeV/c passing our lepton selection, and

- invariant mass with the 2nd-leg objects isin the mass region of 81 through 101 GeV/c^2.

The definition of the 2nd-leg are listed in Table 4.3.

Away the first and the second leading jet

We require the leptons in the jet samples to be away the 1st and 2nd leading jets because the 1st leading jet tend to trigger and the 2nd leading jet may have trigger bias as the 1st leading jet, especially dijet events. Therefore, we choose the leptons with being away these jets:

$$\Delta R = \sqrt{(\Delta\eta)^2 + (\Delta\phi)^2} > 1. \tag{4.3}$$

4.3 Likelihood-Based Lepton Identification

Although the cut-based method is used common at CDF to reduce backgrounds, it is too tight to remain because this method requires all satisfications for candidates. For example, consider the electron candidate. If the candidate fails to *one* ID variable, it is identified as background even if it satisfies all the other ID variables.

Furthermore, if backgrounds satisfy all ID variables as the same of signal, this means that these backgrounds can not be distinguished from signal because no more information in the cut-based method.

Likelihood-based identification, however, compensates both those deficits. We use this method to the lepton identification (Likelihood-based lepton identification, LLID) to reduce QCD jet background, which highly contaminates the data.

LLID is simple method, although more complicated than the cut-based. First, we prepare PDFs for each signal and background. Second, we construct likelihood function as single discriminant. Finally, we set the threshold on the likelihood function, and discriminate signal from background.

4.3.1 Probability Distribution Functions for LLID

Probability distribution functions (PDFs) are not related to the parton distribution function, and you should not confuse these.

PDF shows how possible the object is something (in this case, electron, muon, or jet). In this thesis, we construct the binned PDFs by using Z control samples because it is harder to create by fitting. The first and the last bins in each PDF contain the all below and above contents in the region PDF, respectively. The region and the number of bins for PDFs are determined carefully in order to separate signal and background, and not to overestimate. In out of the PDF region, most of candidates are background. As the cut-based method, if the candidate have the probability in the first or last bin in one PDF, it is background with high possibility. Furthermore, because the PDFs have

Event pre-selection	
$\lvert z_{\rm pv}\rvert < 60$ cm	
Cosmic-ray veto	
Electron selection	**Muon selection**
Geometrical and kinematical cuts	
CEM	CMUP or CMX
Fiducial	Fiducial (CMUP), $\rho_{\rm COT} > 140$ cm (CMX)
	Blue-beam veto, keystone veto, miniskirt veto
$E_T^{\ell_1} > 20$ GeV ($p_T > 10$ GeV/c)	$p_T^{\ell_1} > 20$ GeV/c
$E_T^{\ell_2} > 6$ GeV ($p_T > 6$ GeV/c)	$p_T^{\ell_2} > 6$ GeV/c
Track quality cuts	
Axial ≥ 3 and stereo ≥ 3 (≥ 7 hits)	
$\lvert z_0 - z_{\rm pv}\rvert < 2$ cm	
Silicon hits ≥ 3	
$\lvert d_0\rvert < 0.02$ cm	
Isolation cut	
$\mathrm{ISO}_{0.4}^{\rm cal} < 2$ GeV	
Identification cuts	
HAD/EM $< 0.055 + 0.00045 \times E$	EM $< \max(2, 2 + 0.0115 \times (p - 100))$ GeV
$L_{\rm shr} < 0.2$ ($E_T < 70$ GeV)	HAD $< \max(6, 6 + 0.0280 \times (p - 100))$ GeV
$E/p < 2$ ($E_T < 50$ GeV)	$\lvert r \times \Delta\phi\rvert < 3, 5, 6$ cm (CMU, P, X)
$\chi^2_{\rm strip} < 10$	
$\lvert\Delta z_{\rm CES}\rvert < 3$ cm	
$-3.0 < Q \times \Delta x_{\rm CES} < 1.5$ cm	
Other cuts	
Conversion removal	

Table 4.1: Event pre-selection and lepton selection cuts.

the structure in the region, LLID can distinguish signal from background in the region compared to cut-based, which can not (Figure 4.1). PDF should have the normalization condition, that is,

$$\int_{-\infty}^{\infty} \mathrm{d}x \mathrm{PDF}(x) = 1. \tag{4.4}$$

Exactly two leptons
$\lvert z_0^{\ell_1} - z_0^{\ell_2} \rvert < 2$ cm
Dilepton mass > 12 GeV/c^2
Z removal
At least one like-sign pair

Table 4.2: Dilepton selection cuts.

Track object
Opposite-sign
$p_T > 10$ GeV/c
track cone-isolation < 4 GeV/c
axial ≥ 3 and stereo ≥ 2 (≥ 5 hits)
$\lvert z_0 - z_{\rm pv} \rvert < 10$ cm
EM object
$E_T > 10$ GeV
HAD/EM < 0.12
fractional isolation $\mathrm{ISO}_{0.4}^{\rm cal}/E_T < 0.15$
Muon object
$p_T > 10$ GeV/c
EM < 5 GeV
HAD < 10 GeV
fractional isolation $\mathrm{ISO}_{0.4}^{\rm cal}/p_T < 0.15$
$\lvert z_0 - z_{\rm pv} \rvert < 10$ cm
$\lvert d_0 \rvert < 0.5$ cm

Table 4.3: Physics objects used to identify and remove Z bosons.

and we should also operate the normalization to the binned PDFs. These PDFs are shown in Figures 4.2 $\sim$ 4.6.

4.3.2 Likelihood Function

We collect the information of each PDF, and construct signal discriminant as

$$\mathcal{S} = \prod_{i=1}^{n} S_i \tag{4.5}$$

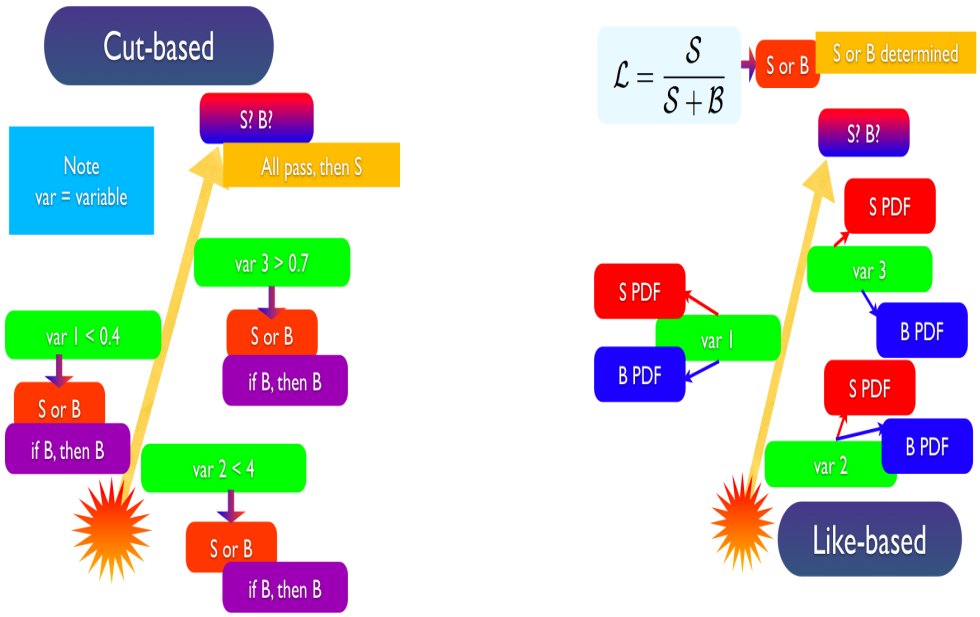

Figure 4.1: Illustration of CLID (the left figure) and LLID(the right figure).

and background

$$\mathcal{B} = \prod_{i=1}^{n} B_i, \tag{4.6}$$

where n is the number of variables, S_i and B_i are the i-th PDF of signal and background, respectively. The construction of the final discriminant is arbitrary, e.g. $\mathcal{S}/\mathcal{B}, \mathcal{S}/(\mathcal{S}+\mathcal{B}), \mathcal{S}/\sqrt{\mathcal{B}}$. In this thesis, we choose the discriminant as

$$\mathcal{L} = \frac{\mathcal{S}}{\mathcal{S}+\mathcal{B}}. \tag{4.7}$$

This is motivated by Neyman-Pearson lemma [34], which claims that a likelihood ratio is the most sensitive variable for separating hypothesis, and the form is also used in [35, 36, 37].

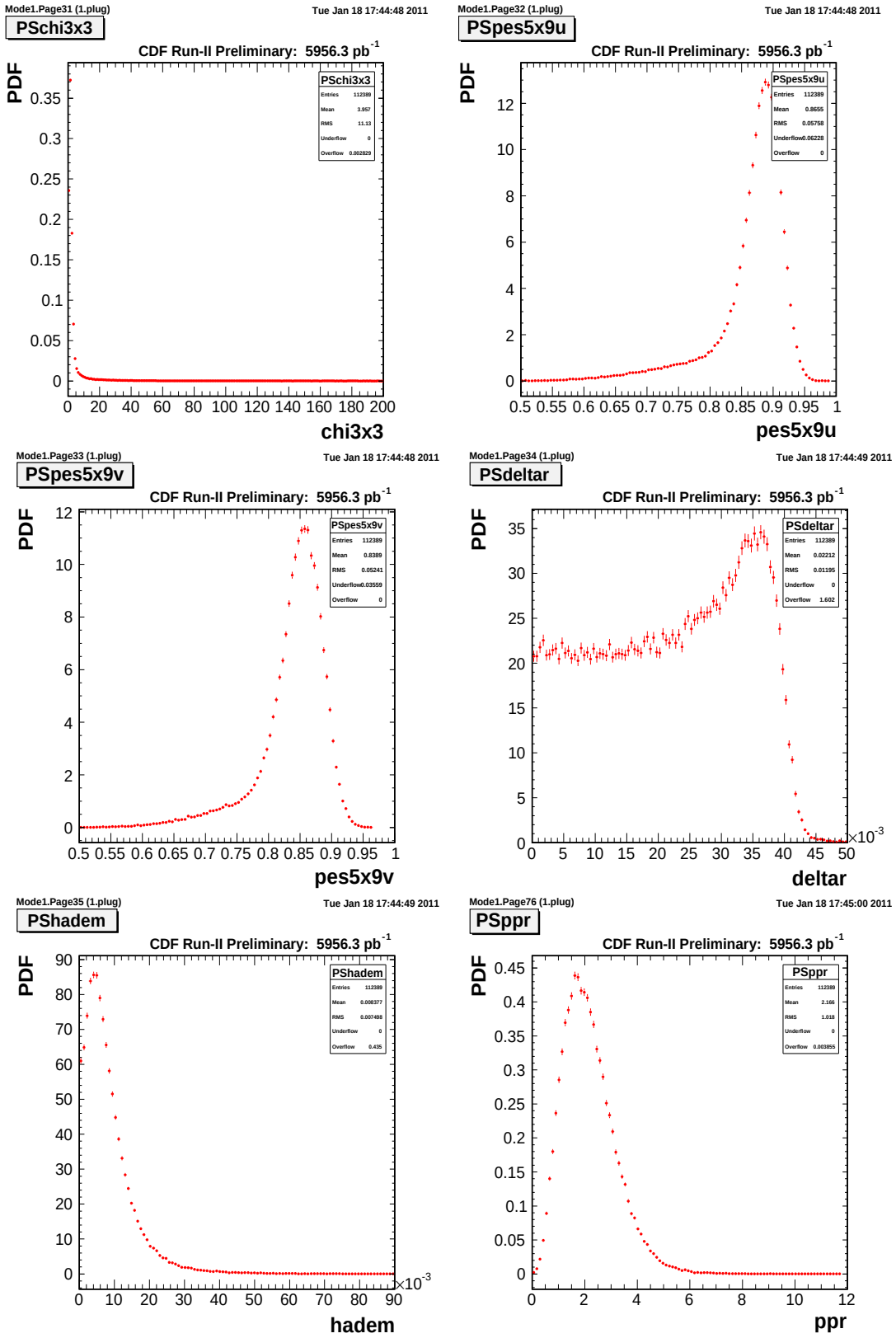

Figure 4.2: Z MC PDFs.

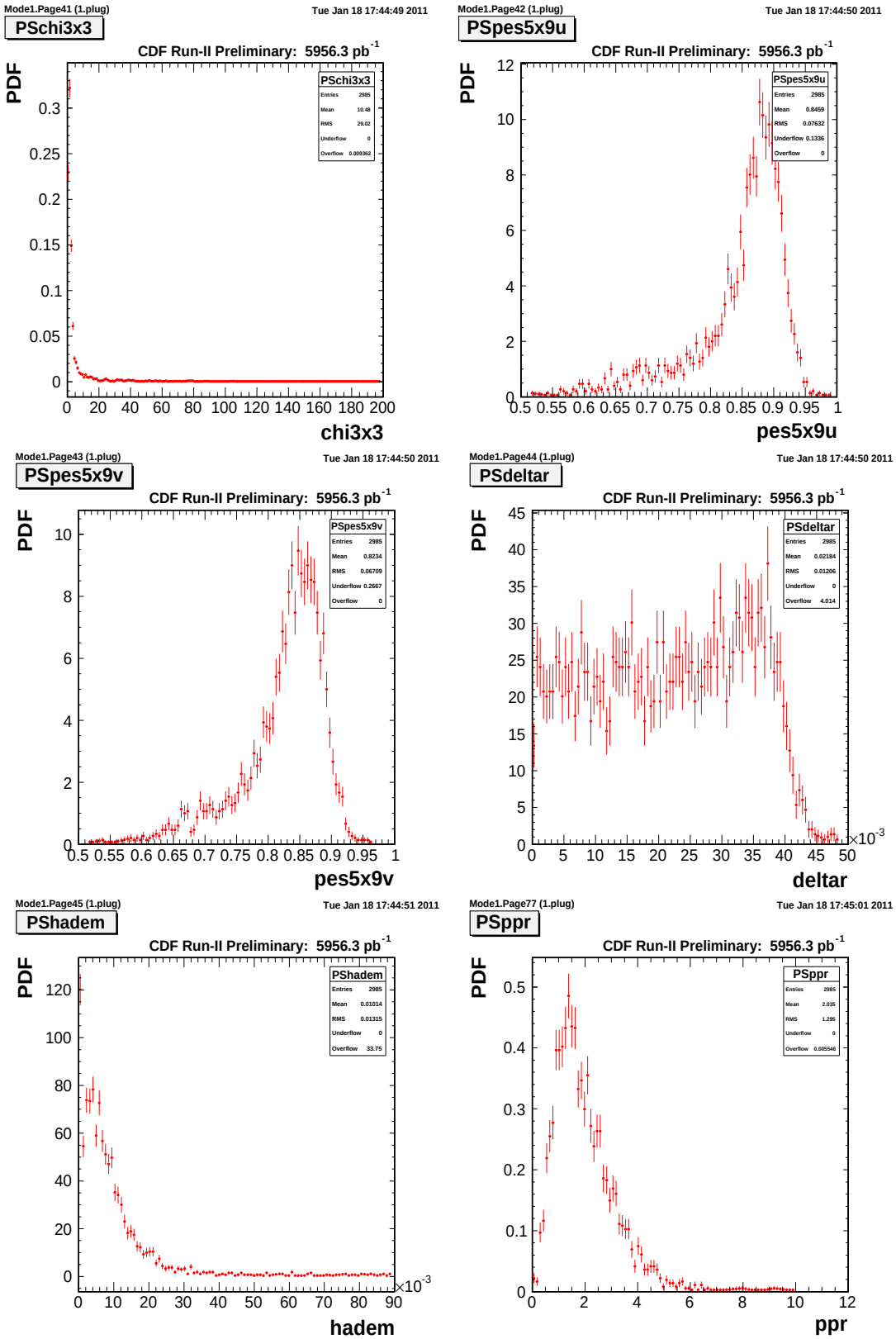

Figure 4.3: Higgs 110 PDFs.

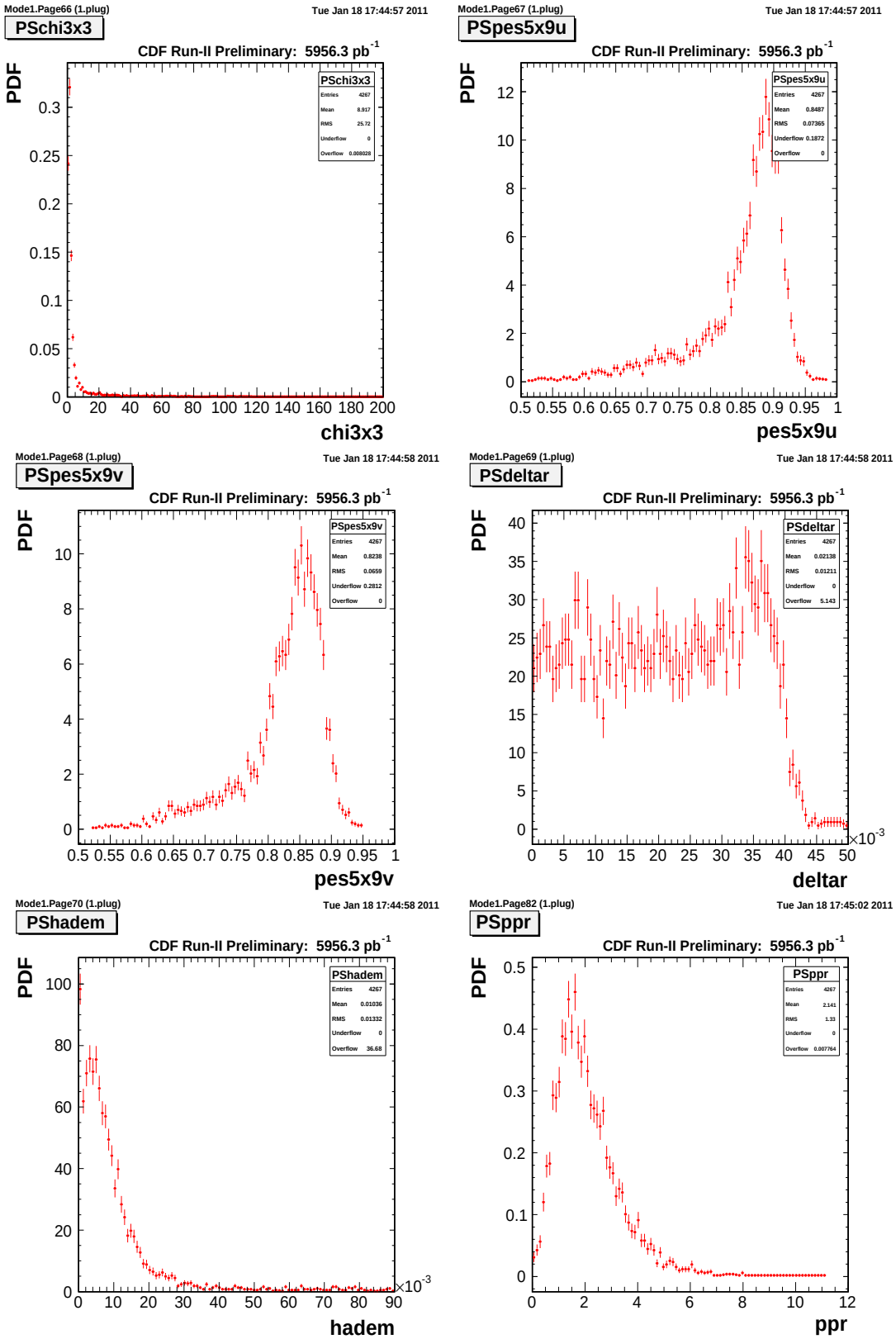

Figure 4.4: Higgs 160 PDFs.

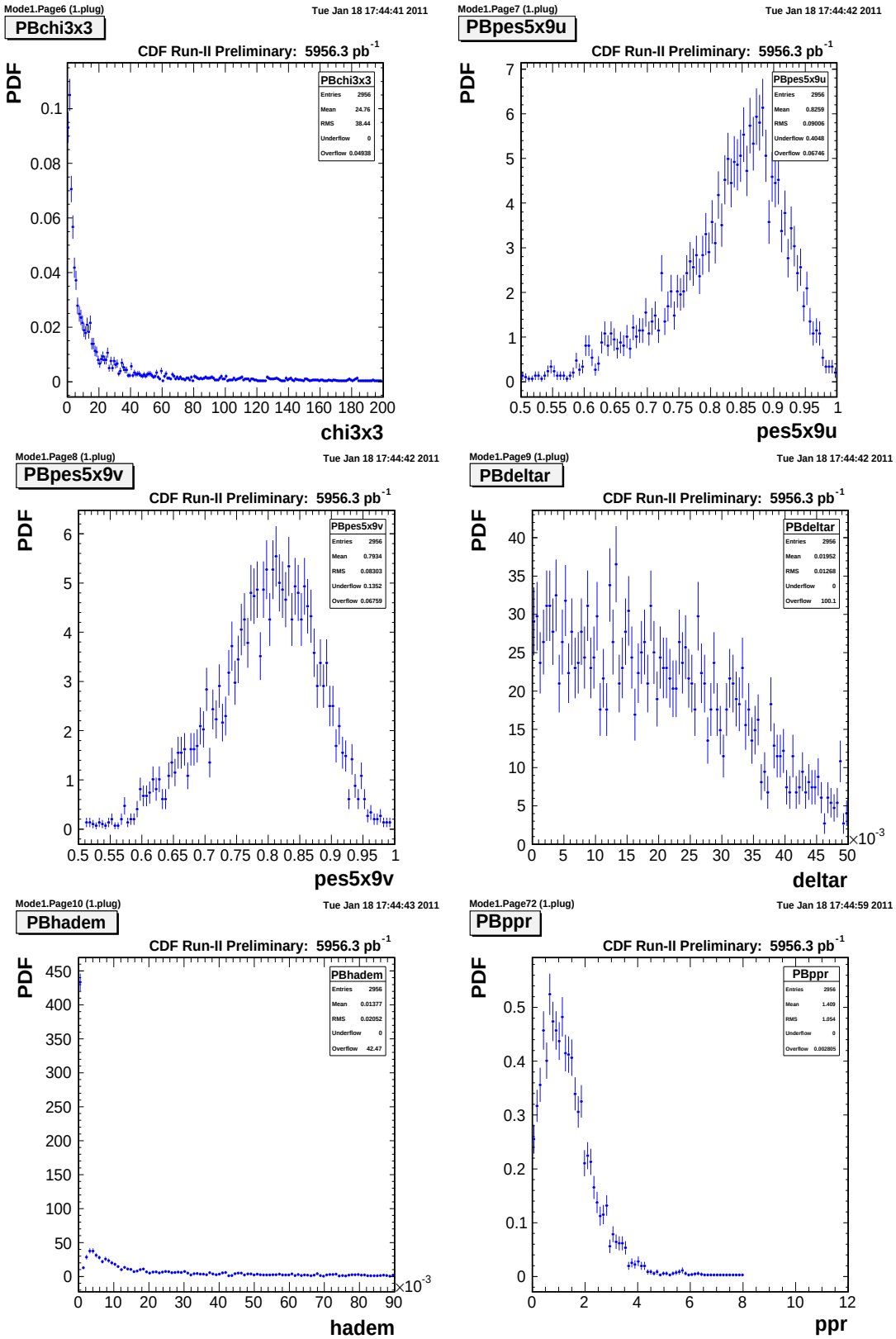

Figure 4.5: Jet 20 PDFs.

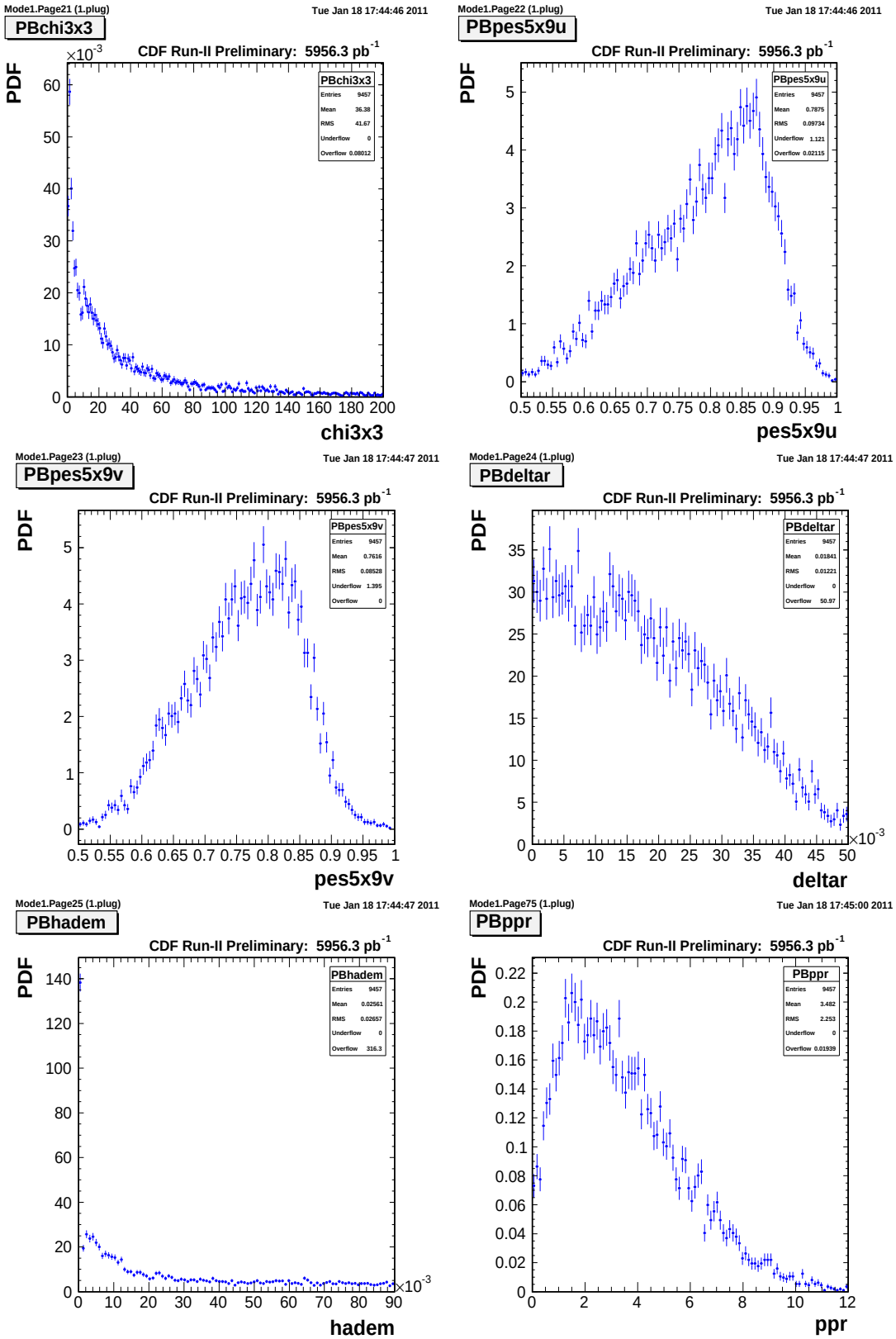

Figure 4.6: Jet 100 PDFs.

Chapter 5

Results and Future Plan

5.1 Improvements compared to the CLID

We estimate efficiencies for both LLID and CLID and compare them. For this purpose, we compare the signal (background) efficiency with adjusting the likelihood cut value in order to be the same background (signal) efficiency for LLID and CLID.

The results show that LLID is better performance than CLID when we use Z Monte Carlo as signal and jet samples by triggered low-E_T jet as background. Higgs Monte Carlo (signal) and jet samples by triggerd high-E_T jet (background) result that CLID is better performance. We consider that kinematics of the high-E_T jets are similar to the electrons from Higgs boson and PDFs used by LLID show little difference between them enough to separate signal from background.

The efficiencies and improvement/reduction are shown in Tables 5.1 $\sim$ 5.36.

Sample	Same background efficiency		
	L cut	El efficiency (ZMC)	Improvement
JT20	0.10	0.9758 ± 0.00004	$\times 1.07$
JT50	0.18	0.9581 ± 0.00006	$\times 1.05$
JT70	0.25	0.9445 ± 0.00008	$\times 1.03$
JT100	0.29	0.9354 ± 0.00010	$\times 1.02$

Table 5.1: The efficiencies for LLID and CLID w/o PPR. The signal PDFs are ZMC and the Background is prescaled jet sample PDFs.

Sample	Same signal efficiency		
	L cut	Jet efficiency (ZMC)	Reduction
JT20	0.37	0.1803 ± 0.00608	$\times 2.10$
JT50	0.37	0.1386 ± 0.00521	$\times 1.67$
JT70	0.37	0.1242 ± 0.00331	$\times 1.36$
JT100	0.37	0.1125 ± 0.00255	$\times 1.20$

Table 5.2: The efficiencies for LLID and CLID w/o PPR. The signal PDFs are ZMC and the Background is prescaled jet sample PDFs.

Sample	Same background efficiency		
	L cut	El efficiency (ZMC)	Improvement
JT20	0.10	0.8809 ± 0.00100	$\times 1.07$
JT50	0.18	0.8492 ± 0.00124	$\times 1.04$
JT70	0.25	0.8264 ± 0.00142	$\times 1.01$
JT100	0.29	0.8127 ± 0.00154	$\times 0.99$

Table 5.3: The efficiencies for LLID and CLID w/o PPR. The signal PDFs are ZMC and the Background is prescaled jet sample PDFs.

Sample	Same signal efficiency		
	L cut	Jet efficiency (ZMC)	Reduction
JT20	0.27	0.2271 ± 0.00621	$\times 1.67$
JT50	0.27	0.1887 ± 0.00547	$\times 1.23$
JT70	0.27	0.1616 ± 0.00350	$\times 1.05$
JT100	0.27	0.1414 ± 0.00268	$\times 0.95$

Table 5.4: The efficiencies for LLID and CLID w/o PPR. The signal PDFs are ZMC and the Background is prescaled jet sample PDFs.

Sample	Same background efficiency		
	L cut	El efficiency (ZMC)	Improvement
JT20	0.10	0.8907 ± 0.00077	$\times 1.08$
JT50	0.18	0.8594 ± 0.00097	$\times 1.05$
JT70	0.25	0.8365 ± 0.00113	$\times 1.02$
JT100	0.29	0.8216 ± 0.00122	$\times 1.00$

Table 5.5: The efficiencies for LLID and CLID w/o PPR. The signal PDFs are ZMC and the Background is prescaled jet sample PDFs.

Sample	Same signal efficiency		
	L cut	Jet efficiency (ZMC)	Reduction
JT20	0.29	0.2193 ± 0.00620	$\times 1.73$
JT50	0.29	0.1727 ± 0.00541	$\times 1.34$
JT70	0.29	0.1529 ± 0.00346	$\times 1.11$
JT100	0.29	0.1347 ± 0.00265	$\times 1.00$

Table 5.6: The efficiencies for LLID and CLID w/o PPR. The signal PDFs are ZMC and the Background is prescaled jet sample PDFs.

Sample	Same background efficiency		
	L cut	El efficiency (Higgs110)	Improvement
JT20	0.26	0.9691 ± 0.00005	$\times 1.06$
JT50	0.43	0.9327 ± 0.00010	$\times 1.02$
JT70	0.54	0.9005 ± 0.00015	$\times 0.99$
JT100	0.60	0.8716 ± 0.00019	$\times 0.95$

Table 5.7: The efficiencies for LLID and CLID w/o PPR. The signal PDFs are Higgs110 and the Background is prescaled jet sample PDFs.

Sample	Same signal efficiency		
	L cut	Jet efficiency (Higgs110)	Reduction
JT20	0.50	0.1949 ± 0.00613	$\times 1.95$
JT50	0.50	0.1928 ± 0.00549	$\times 1.20$
JT70	0.50	0.1877 ± 0.00357	$\times 0.90$
JT100	0.50	0.1796 ± 0.00279	$\times 0.75$

Table 5.8: The efficiencies for LLID and CLID w/o PPR. The signal PDFs are Higgs110 and the Background is prescaled jet sample PDFs.

Sample	Same background efficiency		
	L cut	El efficiency (Higgs110)	Improvement
JT20	0.26	0.9020 ± 0.00082	$\times 1.10$
JT50	0.43	0.8397 ± 0.00131	$\times 1.02$
JT70	0.54	0.7976 ± 0.00167	$\times 0.97$
JT100	0.60	0.7592 ± 0.00192	$\times 0.93$

Table 5.9: The efficiencies for LLID and CLID w/o PPR. The signal PDFs are Higgs110 and the Background is prescaled jet sample PDFs.

Sample	Same signal efficiency		
	L cut	Jet efficiency (Higgs110)	Reduction
JT20	0.48	0.2033 ± 0.00617	$\times 1.87$
JT50	0.48	0.2006 ± 0.00552	$\times 1.15$
JT70	0.48	0.1963 ± 0.00359	$\times 0.86$
JT100	0.48	0.1875 ± 0.00281	$\times 0.72$

Table 5.10: The efficiencies for LLID and CLID w/o PPR. The signal PDFs are Higgs110 and the Background is prescaled jet sample PDFs.

Sample	Same background efficiency		
	L cut	El efficiency (Higgs110)	Improvement
JT20	0.26	0.8985 ± 0.00071	$\times 1.09$
JT50	0.43	0.8392 ± 0.00110	$\times 1.02$
JT70	0.54	0.7942 ± 0.00141	$\times 0.97$
JT100	0.60	0.7571 ± 0.00162	$\times 0.92$

Table 5.11: The efficiencies for LLID and CLID w/o PPR. The signal PDFs are Higgs110 and the Background is prescaled jet sample PDFs.

Sample	Same signal efficiency		
	L cut	Jet efficiency (Higgs110)	Reduction
JT20	0.47	0.2099 ± 0.00618	$\times 1.81$
JT50	0.47	0.2091 ± 0.00554	$\times 1.11$
JT70	0.47	0.2048 ± 0.00361	$\times 0.83$
JT100	0.47	0.1943 ± 0.00282	$\times 0.69$

Table 5.12: The efficiencies for LLID and CLID w/o PPR. The signal PDFs are Higgs110 and the Background is prescaled jet sample PDFs.

Sample	Same background efficiency		
	L cut	El efficiency (Higgs160)	Improvement
JT20	0.23	0.9724 ± 0.00004	$\times 1.06$
JT50	0.42	0.9349 ± 0.00010	$\times 1.02$
JT70	0.52	0.9032 ± 0.00014	$\times 0.99$
JT100	0.59	0.8731 ± 0.00018	$\times 0.96$

Table 5.13: The efficiencies for LLID and CLID w/o PPR. The signal PDFs are Higgs160 and the Background is prescaled jet sample PDFs.

Sample	Same signal efficiency		
	L cut	Jet efficiency (Higgs160)	Reduction
JT20	0.49	0.1824 ± 0.00609	$\times 2.08$
JT50	0.49	0.1850 ± 0.00547	$\times 1.25$
JT70	0.49	0.1845 ± 0.00356	$\times 0.92$
JT100	0.49	0.1782 ± 0.00279	$\times 0.76$

Table 5.14: The efficiencies for LLID and CLID w/o PPR. The signal PDFs are Higgs160 and the Background is prescaled jet sample PDFs.

Sample	Same background efficiency		
	L cut	El efficiency (Higgs160)	Improvement
JT20	0.23	0.8941 ± 0.00090	$\times 1.09$
JT50	0.42	0.8305 ± 0.00142	$\times 1.01$
JT70	0.52	0.7832 ± 0.00176	$\times 0.96$
JT100	0.59	0.7389 ± 0.00207	$\times 0.90$

Table 5.15: The efficiencies for LLID and CLID w/o PPR. The signal PDFs are Higgs160 and the Background is prescaled jet sample PDFs.

Sample	Same signal efficiency		
	L cut	Jet efficiency (Higgs160)	Reduction
JT20	0.43	0.2148 ± 0.00620	$\times 1.77$
JT50	0.43	0.2166 ± 0.00556	$\times 1.07$
JT70	0.43	0.2111 ± 0.00362	$\times 0.80$
JT100	0.43	0.2044 ± 0.00283	$\times 0.66$

Table 5.16: The efficiencies for LLID and CLID w/o PPR. The signal PDFs are Higgs160 and the Background is prescaled jet sample PDFs.

Sample	Same background efficiency		
	L cut	El efficiency (Higgs160)	Improvement
JT20	0.23	0.9189 ± 0.00058	$\times 1.12$
JT50	0.42	0.8549 ± 0.00102	$\times 1.04$
JT70	0.52	0.8108 ± 0.00129	$\times 0.99$
JT100	0.59	0.7744 ± 0.00151	$\times 0.94$

Table 5.17: The efficiencies for LLID and CLID w/o PPR. The signal PDFs are Higgs160 and the Background is prescaled jet sample PDFs.

Sample	Same signal efficiency		
	L cut	Jet efficiency (Higgs160)	Reduction
JT20	0.49	0.1816 ± 0.00609	$\times 2.09$
JT50	0.49	0.1840 ± 0.00547	$\times 1.26$
JT70	0.49	0.1834 ± 0.00356	$\times 0.92$
JT100	0.49	0.1771 ± 0.00279	$\times 0.76$

Table 5.18: The efficiencies for LLID and CLID w/o PPR. The signal PDFs are Higgs160 and the Background is prescaled jet sample PDFs.

Sample	Same background efficiency		
	L cut	El efficiency (ZMC)	Improvement
JT20	0.06	0.9897 ± 0.00002	$\times 1.08$
JT50	0.17	0.9676 ± 0.00005	$\times 1.06$
JT70	0.25	0.9521 ± 0.00007	$\times 1.04$
JT100	0.31	0.9413 ± 0.00009	$\times 1.03$

Table 5.19: The efficiencies for LLID and CLID w/ PPR. The signal PDFs are ZMC and the Background is prescaled jet sample PDFs.

Sample	Same signal efficiency		
	L cut	Jet efficiency (ZMC)	Reduction
JT20	0.44	0.1212 ± 0.00410	$\times 3.47$
JT50	0.44	0.1156 ± 0.00399	$\times 2.14$
JT70	0.44	0.1157 ± 0.00270	$\times 1.57$
JT100	0.44	0.1026 ± 0.00209	$\times 1.35$

Table 5.20: The efficiencies for LLID and CLID w/ PPR. The signal PDFs are ZMC and the Background is prescaled jet sample PDFs.

Sample	Same background efficiency		
	L cut	El efficiency (ZMC)	Improvement
JT20	0.06	0.9118 ± 0.00079	$\times 1.11$
JT50	0.17	0.8466 ± 0.00127	$\times 1.03$
JT70	0.25	0.8196 ± 0.00148	$\times 1.00$
JT100	0.31	0.8008 ± 0.00163	$\times 0.98$

Table 5.21: The efficiencies for LLID and CLID w/ PPR. The signal PDFs are ZMC and the Background is prescaled jet sample PDFs.

Sample	Same signal efficiency		
	L cut	Jet efficiency (ZMC)	Reduction
JT20	0.25	0.1953 ± 0.00445	$\times 2.15$
JT50	0.25	0.1961 ± 0.00440	$\times 1.26$
JT70	0.25	0.1831 ± 0.00295	$\times 0.99$
JT100	0.25	0.1600 ± 0.00231	$\times 0.87$

Table 5.22: The efficiencies for LLID and CLID w/ PPR. The signal PDFs are ZMC and the Background is prescaled jet sample PDFs.

Sample	Same background efficiency		
	L cut	El efficiency (ZMC)	Improvement
JT20	0.06	0.9138 ± 0.00064	$\times 1.11$
JT50	0.17	0.8647 ± 0.00096	$\times 1.05$
JT70	0.25	0.8347 ± 0.00114	$\times 1.02$
JT100	0.31	0.8173 ± 0.00125	$\times 0.99$

Table 5.23: The efficiencies for LLID and CLID w/ PPR. The signal PDFs are ZMC and the Background is prescaled jet sample PDFs.

Sample	Same signal efficiency		
	L cut	Jet efficiency (ZMC)	Reduction
JT20	0.29	0.1745 ± 0.00439	$\times 2.41$
JT50	0.29	0.1764 ± 0.00434	$\times 1.40$
JT70	0.29	0.1638 ± 0.00291	$\times 1.11$
JT100	0.29	0.1443 ± 0.00227	$\times 0.96$

Table 5.24: The efficiencies for LLID and CLID w/ PPR. The signal PDFs are ZMC and the Background is prescaled jet sample PDFs.

Sample	Same background efficiency		
	L cut	El efficiency (Higgs110)	Improvement
JT20	0.19	0.9853 ± 0.00002	$\times 1.08$
JT50	0.46	0.9394 ± 0.00009	$\times 1.03$
JT70	0.60	0.8968 ± 0.00015	$\times 0.98$
JT100	0.71	0.8436 ± 0.00023	$\times 0.92$

Table 5.25: The efficiencies for LLID and CLID w/ PPR. The signal PDFs are Higgs110 and the Background is prescaled jet sample PDFs.

Sample	Same signal efficiency		
	L cut	Jet efficiency (Higgs110)	Reduction
JT20	0.56	0.1416 ± 0.00423	$\times 2.97$
JT50	0.56	0.1849 ± 0.00437	$\times 1.34$
JT70	0.56	0.2127 ± 0.00300	$\times 0.86$
JT100	0.56	0.2265 ± 0.00240	$\times 0.61$

Table 5.26: The efficiencies for LLID and CLID w/ PPR. The signal PDFs are Higgs110 and the Background is prescaled jet sample PDFs.

Sample	Same background efficiency		
	L cut	El efficiency (Higgs110)	Improvement
JT20	0.19	0.9365 ± 0.00054	$\times 1.14$
JT50	0.46	0.8378 ± 0.00133	$\times 1.02$
JT70	0.60	0.7736 ± 0.00181	$\times 0.94$
JT100	0.71	0.7067 ± 0.00230	$\times 0.86$

Table 5.27: The efficiencies for LLID and CLID w/ PPR. The signal PDFs are Higgs110 and the Background is prescaled jet sample PDFs.

Sample	Same signal efficiency		
	L cut	Jet efficiency (Higgs110)	Reduction
JT20	0.51	0.1664 ± 0.00436	$\times 2.53$
JT50	0.51	0.2152 ± 0.00444	$\times 1.15$
JT70	0.51	0.2425 ± 0.00302	$\times 0.75$
JT100	0.51	0.2570 ± 0.00241	$\times 0.54$

Table 5.28: The efficiencies for LLID and CLID w/ PPR. The signal PDFs are Higgs110 and the Background is prescaled jet sample PDFs.

Sample	Same background efficiency		
	L cut	El efficiency (Higgs110)	Improvement
JT20	0.19	0.9294 ± 0.00050	$\times 1.13$
JT50	0.46	0.8411 ± 0.00109	$\times 1.02$
JT70	0.60	0.7706 ± 0.00153	$\times 0.94$
JT100	0.71	0.7069 ± 0.00192	$\times 0.86$

Table 5.29: The efficiencies for LLID and CLID w/ PPR. The signal PDFs are Higgs110 and the Background is prescaled jet sample PDFs.

Sample	Same signal efficiency		
	L cut	Jet efficiency (Higgs110)	Reduction
JT20	0.50	0.1693 ± 0.00438	$\times 2.48$
JT50	0.50	0.2211 ± 0.00445	$\times 1.12$
JT70	0.50	0.2479 ± 0.00302	$\times 0.73$
JT100	0.50	0.2623 ± 0.00241	$\times 0.53$

Table 5.30: The efficiencies for LLID and CLID w/ PPR. The signal PDFs are Higgs110 and the Background is prescaled jet sample PDFs.

Sample	Same background efficiency		
	L cut	El efficiency (Higgs160)	Improvement
JT20	0.17	0.9866 ± 0.00002	$\times 1.08$
JT50	0.44	0.9412 ± 0.00009	$\times 1.03$
JT70	0.62	0.8888 ± 0.00017	$\times 0.97$
JT100	0.72	0.8366 ± 0.00024	$\times 0.92$

Table 5.31: The efficiencies for LLID and CLID w/ PPR. The signal PDFs are Higgs160 and the Background is prescaled jet sample PDFs.

Sample	Same signal efficiency		
	L cut	Jet efficiency (Higgs160)	Reduction
JT20	0.55	0.1364 ± 0.00418	$\times 3.08$
JT50	0.55	0.1787 ± 0.00434	$\times 1.38$
JT70	0.55	0.2215 ± 0.00301	$\times 0.82$
JT100	0.55	0.2436 ± 0.00241	$\times 0.57$

Table 5.32: The efficiencies for LLID and CLID w/ PPR. The signal PDFs are Higgs160 and the Background is prescaled jet sample PDFs.

Sample	Same background efficiency		
	L cut	El efficiency (Higgs160)	Improvement
JT20	0.17	0.9256 ± 0.00064	$\times 1.13$
JT50	0.44	0.8242 ± 0.00144	$\times 1.00$
JT70	0.62	0.7418 ± 0.00210	$\times 0.90$
JT100	0.72	0.6713 ± 0.00256	$\times 0.82$

Table 5.33: The efficiencies for LLID and CLID w/ PPR. The signal PDFs are Higgs160 and the Background is prescaled jet sample PDFs.

Sample	Same signal efficiency		
	L cut	Jet efficiency (Higgs160)	Reduction
JT20	0.45	0.1842 ± 0.00443	$\times 2.28$
JT50	0.45	0.2379 ± 0.00446	$\times 1.04$
JT70	0.45	0.2834 ± 0.00301	$\times 0.64$
JT100	0.45	0.3091 ± 0.00238	$\times 0.45$

Table 5.34: The efficiencies for LLID and CLID w/ PPR. The signal PDFs are Higgs160 and the Background is prescaled jet sample PDFs.

Sample	Same background efficiency		
	L cut	El efficiency (Higgs160)	Improvement
JT20	0.17	0.9474 ± 0.00038	$\times 1.15$
JT50	0.44	0.8587 ± 0.00098	$\times 1.04$
JT70	0.62	0.7769 ± 0.00154	$\times 0.95$
JT100	0.72	0.7150 ± 0.00189	$\times 0.87$

Table 5.35: The efficiencies for LLID and CLID w/ PPR. The signal PDFs are Higgs160 and the Background is prescaled jet sample PDFs.

Sample	Same signal efficiency		
	L cut	Jet efficiency (Higgs160)	Reduction
JT20	0.52	0.1531 ± 0.00428	$\times 2.74$
JT50	0.52	0.1932 ± 0.00439	$\times 1.28$
JT70	0.52	0.2385 ± 0.00302	$\times 0.76$
JT100	0.52	0.2625 ± 0.00241	$\times 0.53$

Table 5.36: The efficiencies for LLID and CLID w/ PPR. The signal PDFs are Higgs160 and the Background is prescaled jet sample PDFs.

5.2 Conclusions

We have estimated lepton selection identification efficiencies for the LLID with fixing the same signal or background efficiency as the CLID. In these, we emphasize that the background reduction factor is 3.47 times larger than the CLID with plug preradiator information. It is the remarkable result because our search Higgs channel, $Wh \to WWW \to \ell^{\pm}\ell^{\pm} + X$, forces us to estimate fake lepton as dominant background.

Unfortunately, Tevatron determined that the run ends in 2011, and there is no Run III. However, we have many data to be analyzed by many people, and the hot environment with discussing each other in Tevatron is expected to continue to the next several years.

5.3 Future Plan

We want to discover Higgs boson, and therefore, we add electrons in the plug region and apply LLID to reduce backgrounds compared to CLID. However, we are faced to many things to do. Here, we list up them we have to do to estimate new backgrounds components, or we want to do to get large sensitivity.

5.3.1 Charge Mismeasurements

In the previous analysis, we did not include these factor as backgounds because in the central region we can neglect them when we require the fiducial region and silicon and COT hits. In contrast to the central region, we think that we have to consider charge mismeasurements in the plug region because of poorer detectors than the central. We plan to these rates by using Z control samples with subtracting γ^* events. Perhaps, we have to deduce these with depending the number of Silicon hits, COT hits, or $|\eta|$.

5.3.2 Multivariate Analysis

In general, we want to separate signal and backgrounds maximally. we usually operate this by using Bayesian classification,

$$P(Class = C|y) = \frac{P(y|C) \cdot P(C)}{P(y)} \tag{5.1}$$

where $P(Class = C|y)$ is the probability that this belongs to the Class C given the variable set y, $P(y|C)$ is the likelihood, P(C) is prior probability, and $P(y)$ is the normalization factor. If we want to classify events into two groups, signal and background, it is based on the equation:

$$\frac{P(S|y)}{P(B|y)} = \frac{P(y|S)}{P(y|B)} \cdot \frac{P(S)}{P(B)} \tag{5.2}$$

where $P(S|y)/P(B|y)$ is the posterior odds ratio and this determines the event is signal and background.

Basically, we operate this by choose "one" dimension corresponding y in the above equation. This corresponds to the function $\mathcal{F}$ such that

$$\mathcal{F} : \mathbb{R}^N \to \mathbb{R}, \tag{5.3}$$

where $\mathbb{R}^N$ represents the variable space to characterize signal or background, which we call feature space, N is the number of the variables. Therefore, we can divide two tasks to distinguish them.

- One is to find which is good variable(s) to characterize signal or backgrounds.
- The other is to find the function $\mathcal{F}$ to separate them maximally in one dimension.

We expect the discriminant variable based on the matrix element method as the former candidate. The matrix element method is described in Appendix A.

For the latter case, we have good tools provided by TMVA [38, 39]. Most of these tools are using supervised (machine) learning. For now, we have implemented boosted decision tree method (BDT) in the previous analysis [40]. Therefore, we use BDT if we can treat more than two backgrounds simultaneously, which corresponds to the situation that there are only two class type, signal or background, or use BDTG if there are multiclasses ($class = \text{class A}, \text{class B}, \text{class C}, \dots$).

Appendix A

The Matrix Element Method

$WH \rightarrow WWW$ like-sign dilepton analysis rejects many QCD jets for the charge requirement. However, we have to treat the like-sign dilepton coming from the physical backgrounds, WZ and ZZ, and these are not negligible.

We want to separate between signal events and background significantly. This process can be divided by two categories: one is to find variables showing large differences between signal and background (here, we define this space as variable space by convention), and the other is to find the function which transmits the characteristic space (normally 1 dimensional space) to discriminate signal from background effectively. The latter method is developed by many people, and there are many multivariate methods now, for example, boosted decision tree (BDT), neural network (NN), support vector machine (SVM). However, the former is also important to discriminate these because multivariate methods use variable space information. If we find the most effective variable, then it means that we can separate these effectively, and expect to more separation by using multivariate methods.

The matrix element method, which originally used in DØ analysis [41, 42] or in CDF e.g. [35], is different from the other variables, e.g. 2nd p_T, in respect to using the all kinematical information.

A.1 The Differential Cross Section

The matrix element method is based on the Fermi's golden rule. For the scattering of the initial two particles with four-momenta q_1 and q_2 into n particles with four-momenta p_n, the differential cross sections is given by

$$d\sigma = |\mathcal{M}|^2 \frac{\hbar^2 S}{4\sqrt{(q_1 \cdot q_2)^2 - (m_1 m_2 c^2)^2}} d\Phi_n, \tag{A.1}$$

where S is a combinatoric factor for identical particles, m_i is the particle mass,

$$d\Phi_n = \delta \left(q_1 + q_2 - \sum_{i=1}^{n} p_i \right) \prod_{i=1}^{n} \frac{c d^3 p_i}{(2\pi)^3 2E_i} \tag{A.2}$$

is the phase space factor, and $\mathcal{M}$ is the matrix element for the interaction. If we know all the final state 4-momenta and matrix element exactly, we could obtain the exact differential cross section. However, this is just ideal because we can not estimate the energies of the quarks due to the finite resolution, not calculate exact matrix element due to perturbation theory, and so on. Hence, we need to connect the theoretical consideration to the real world.

A.2 Parton Distribution Functions

We accelerate protons and antiprotons, which are composed of valence quarks, sea quarks and gluons. However, we can not estimate the rate of the quark which we want to know to the protons or anti-protons by calculations.

The Coordinated Theoretical-Experimental Project on QCD (CTEQ), based on the various experiments, provides the parton distribution functions (PDFs) if we input the Bjorken's variable x and the momentum transfer Q^2. In this thesis, we use CTEQ5L PDFs (L means leading order), and the parameters are $\alpha_s = 0.127(\mathrm{Mz})$, $\lambda_4 = 192$ and $\lambda_5 = 146$. We embed the information to the ideal differential cross section formula, and the formula changes to

$$d\sigma = |\mathcal{M}|^2 \frac{\hbar^2 S f(q_1) f(q_2)}{4\sqrt{(q_1 \cdot q_2)^2 - (m_1 m_2 c^2)^2}} d\Phi_n, \tag{A.3}$$

where $f(q_1)$ and $f(q_2)$ are PDFs with Q^2 dependence.

A.3 Transfer Functions

We could not estimate the jet energy precisely due to finite resolutions of the detectors, or not estimate the neutrino information due to missing particles for us. Therefore, we need to input transfer function $W(x, y)$, which connects the detector information x to the parton information y. The function has the *"probability"* meaning, that is,

$$\int \mathrm{d}y W(x, y) = 1, \tag{A.4}$$

which means that the parton variables must exist in the range.

There are three prominent types in transfer functions.

1. Delta Function.
   For electrons and muons, we think its energy and directions can be measured at very high precision. We can apply delta functions by assuming that electrons and muons do not lose their energies so much. Of course, delta function satisfies the normalization condition, that is, in one dimension case,

$$\int_{y_{min}}^{y_{max}} \mathrm{d}y \delta(y - x) = 1 \tag{A.5}$$

if $y_{min} \leq x \leq y_{max}$.

2. Normal Distribution Function.
   In $WH \rightarrow WWW$ like-sign dilepton analysis, we do not need this type. However, the analysis using jets need this type because jet direction can be measured at high precision, but its energy could not due to its fragmentation, calorimeter resolution.

3. Constant.
   We have to apply this type to neutrinos and missing particles. This constant, however, includes many difficulties due to integration in kinematically allowed space.

A.4 Phase Space

Phase space term includes differential ingoing and outgoing particle momenta in momentum space. This gives

$$d\sigma = |\mathcal{M}|^2 \frac{\hbar^2 S f(q_1) f(q_2)}{4\sqrt{(q_1 \cdot q_2)^2 - (m_1 m_2 c^2)^2}} W(x, p(y)) \prod_{i=1}^{N} \frac{c d^3 p_i}{(2\pi)^3 2E_i} \delta(q_1 + q_2 - \sum_{i=1}^{N} p_i), \quad \text{(A.6)}$$

where W(x,p) is the transfer funcion and the second slot indicates the parton information; in this case, p. We can neglect the initial quark masses in most cases, so this equation becomes

$$d\sigma = |\mathcal{M}|^2 \frac{\hbar^2 S f(q_1) f(q_2)}{|q_1||q_2|} W(x, p) \prod_{i=1}^{N} \frac{d^3 p_i}{E_i} \delta(q_1 + q_2 - \sum_{i=1}^{N} p_i). \quad \text{(A.7)}$$

In this equation, we neglect the numerical factors. As we discuss later, it is not important and does not affect our final discriminant.

Here, we write $Wh \rightarrow WWW \rightarrow \ell^{\pm}\ell^{\pm}\nu\nu X_1 X_2$ case:

$$\mathrm{d}\sigma = \frac{|\mathcal{M}|^2 f(q_1) f(q_2)}{|q_1||q_2|} W(x, p) \frac{\mathrm{d}^3 \boldsymbol{p}_{l_1}}{E_{l_1}} \frac{\mathrm{d}^3 \boldsymbol{p}_{\nu_1}}{E_{\nu_1}} \frac{\mathrm{d}^3 \boldsymbol{p}_{l_2}}{E_{l_2}} \frac{\mathrm{d}^3 \boldsymbol{p}_{\nu_2}}{E_{\nu_2}} \frac{\mathrm{d}^3 \boldsymbol{p}_{X_1}}{E_{X_1}} \frac{\mathrm{d}^3 \boldsymbol{p}_{X_2}}{E_{X_2}}. \quad \text{(A.8)}$$

A.5 Combinatoric Issues

In $Wh \rightarrow WWW \rightarrow \ell^{\pm}\ell^{\pm}\nu\nu X_1 X_2$, we can not know which lepton comes from $H \rightarrow WW$. Therefore, we need to consider the all combination and average these cross section.

A.6 Matrix Element

Differential cross section indicates how possible these process occurs. In other words, differential cross section has the *"frequency"*. However, it does not mean that the differential cross section is the probability becasuse probability satisfies normalization condition. There, we adopt the total cross section as the normalization condition. It is a natural selection because total cross section also have the frequency compared to the other processes.

Therefore, the probability which indicates how possibly the process occurs is

$$P_{Wh\to WWW} = \frac{\mathrm{d}\sigma}{\sigma_{tot}} \tag{A.9}$$

where σ_{tot} is the total cross section of $Wh\to WWW\to\ell\ell + X$.

A.7 Numerical Integration

We input the outgoing like-sign dilepton 4 momenta to calculate the differential cross section and the remaining 4 momenta should be integrated. For the simple consideration, we need to integrate over $(4 \times (8-2)) = 24$ dimensions. However, we impose some conditions to this and reduce the dimensions.

- All ingoing and outgoing masses are negligible.
  We do not think the initial and final partons include heavy particle like top quark. It gives the simple energy-momentum relation:

$$E = \sqrt{p_x^2 + p_y^2 + p_z^2}. \tag{A.10}$$

- Initial transverse momenta are negligible.
  In proton or antiproton, quarks and gluons have their own momenta. Of course, these particles have non-zero p_x and p_y components. However, these are negligible compared to the p_z because the parent proton or antiproton is boosted in z direction and valence and sea quarks and gluons have large momenta in z.

- Energy and momentum is conserved in the process.
  These conditions reduce 4 integrational dimensions.

Therefore, our input variable is $\boldsymbol{p}_{l_1}$ and $\boldsymbol{p}_{l_2}$ (6 components) and integrational dimension is

$$\begin{aligned}(\#\text{ of dimension}) &= (4-1)\times(8-2) - 4(\text{Energy-momentum conservation}) \\ &\quad - 2\times 2(\text{Neglect initial transverse momenta}) \\ &= 10.\end{aligned} \tag{A.11}$$

10 dimensions are very large and we rely on numerical integration method. Cuba, a library for multidimensional numerical integration [43, 44], includes 4 integration methods: Vegas, Suave, Divonne, and Cuhre. These integration methods use not only Monte Carlo method (Vegas, Suave, Divonne), but also deterministic method (Divonne, Cuhre).

A.8 Discriminant Based on the Matrix Element

We can construct the matrix element, and the probability for $Wh \to WWW$ process in each event. In the same manner, we can deduce the probability for WZ and ZZ. We want to discriminate Wh from WZ/ZZ, and we construct the discriminant $Dis_{(ME)}$ as

$$\begin{aligned} Dis_{(ME)} &= \frac{S}{S+B} = \frac{P_{Wh}}{P_{(Wh)} + P_{(WZ)} + P_{(ZZ)}} \\ &= \frac{\left(\frac{d\sigma}{\sigma_{tot}}\right)_{Wh}}{\left(\frac{d\sigma}{\sigma_{tot}}\right)_{Wh} + \left(\frac{d\sigma}{\sigma_{tot}}\right)_{WZ} + \left(\frac{d\sigma}{\sigma_{tot}}\right)_{ZZ}}. \end{aligned} \tag{A.12}$$

This form is the same as the likelihood and influenced by Pearson-Neyman theorem.

A.9 Difficulties of Matrix Element Method

For now, we state only good aspects of matrix method. Here, we need to show some difficulties to operate this method. Of course, the list here must be resolved in the future.

A.9.1 Selection of Integration Variables

We are free how to choose the integration variables. Candidates are, we think, simple 3-momenta in Cartesian coordinates (p_i^x, p_i^y, p_i^z), spherical corrdinates $(|p_i|, \theta_i, \phi_i)$, mass of W, and mass of Higgs. There are many candidates in the world, but we must consider that we can operate the integration with ease, time to integrate, stability, and convergence.

3-momenta in Cartesian Coordinates

This variable is very simple and naive selection. This selection, however, has very large area to integrate and difficult to converge the integration even if the deterministic integration. We do not want to this variable to all 3-momenta, but we have to choose this for z momentum of the final outgoing parton to integrate. The final outgoing parton is convention here and comes from the assymetry of transverse and longitudinal

informaition of partons. As we showed previously, we can neglect the initial transverse momenta. Then, we can construct the final transverse momentum by summing the transverse momenta of the rest outgoing partons. But the longitudinal component is not determined, so we have to input this.

3-momenta in Spherical Coordinates

This choice reduce the integration region of the previous selection to some extent. We think that this is useful for the broad decay width and can not apply to Higgs event ($\Gamma \sim 10^{-3}$ GeV). The narrow width means that the non-zero integration area is localized and we do not get the correct result because we have to integrate the most area to return zero value and can not estimate the localized non-zero area.

Mass of W and Higgs

This selection is the most reasonable and appropriate to integrate the $Wh \to WWW$ case. We want to integrate one Higgs mass and two W mass because the other W mass can be estimated by energy-momentum conservation.

Therefore, we think that one Higgs mass, two W mass, two 3-momenta in sperical coordinates and two zenith and azimuthal angles (the radial component is estimated from W mass) and one z component in Cartesian coordinates.

A.9.2 Interpretation of Transfer Function

Transfer function is the bridge between the detector information and the parton level information. There are two standpoints of interpreting this: one is *"parton → detector"* and the other is *"detector → parton"*. For electrons or muons, the form is delta-function and it is no problem. However, for neutrinos and missing particles which we could not observe, we apply the transfer function as the constant (the latter standpoint) or PDF estimated by Monte Carlo (the former standpoint).

We do not know which standpoint is appropriate for this analysis.

A.9.3 Total Cross Section Estimation

Total cross section is difficult to estimate because two like-sign dilepton is integration variables and we calculate this in 16 dimensions. The alternative method is to estimate this from theory, but it does not include detector crack or our analysis cuts.

We are seeking the solution for this.

Bibliography

[1] The TEVNPH Working Group. *"Combined CDF and D0 Upper Limits on Standard Model Higgs-Boson Production with up to 6.7* fb^{-1} *of Data"*. *FERMILAB-CONF-10-257-E*, 2010. ix, 14, 15

[2] Manuel Drees. *"Theory and Phenomenology of Sparticles: An Account of Four-Dimensional N=1 Supersymmetry in High Energy Physics"*. World Scientific Publishing Company, 2005. 1

[3] V. Barger, et al. *"Report of the SUGRA Working Group for Run II of the Tevatron"*. arXiv:hep-ph/0003154v1. 1

[4] Ian J. R. Aitchison and Anthony J. G. Hey. *"Gauge Theories in Particle Physics, Volume I: From Relativistic Quantum Mechanics to QED"*. Taylor & Francis, 3rd edition, 2004. 1

[5] Ian J. R. Aitchison and Anthony J. G. Hey. *"Gauge Theories in Particle Physics, Volume II: QCD and the Electroweak Theory"*. Taylor & Francis, 3rd edition, 2004. 1, 3

[6] Michael E. Peskin and Daniel V. Schroeder. *"An Introduction to Quantum Field Theory"*. Westview Press, 1995. 1

[7] Franz Mandl and Graham Shaw. *"Quantum Field Theory"*. Wiley, 2nd edition, 2010. 1

[8] Francis Halzen and Alan D. Martin. *"Quarks and Leptons: An Introductory Course in Modern Particle Physics"*. Wiley, 1984. 1

[9] Howard Georgi. *"Lie Algebras in Particle Physics: From Isospin to Unified Theories"*. Westview Press, 2nd edition, 1999. 3

[10] P.C. Bhat, H.B. Prosper, and S.S. Snyder. *"Top Quark Physics At The Tevatron"*. arXiv:hep-ex/9809011. 13

[11] The ALEPH, CDF, DØ, DELPHI, L3, OPAL, SLD Collaboration, the LEP Electroweak working Group, the Tevatron Electroweak Group, and the SLD electroweak ans heavy flavour groups. *"Precision Electroweak Measurements and Constraints on the Standard Model"*. arXiv:hep-ex/0811.4682. 13

[12] The LEP Higgs Working Group, ALEPH Collaboration, DELPHI Collaboration, L3 Collaboration, and OPAL Collaboration. *"Search for the Standard Model Higgs boson at LEP". Phys. Lett. B* **565** *(2003) 61-75.* 13

[13] The CDF II Collaboration. *"The CDF II Detector Techinical Design Report". FERMILAB-Pub-96/390-E*, 1996. 20, 30

[14] I. K. Nelson, et al. *"The CDF Layer 00 Detector". FERMILAB-CONF-01/357-E*, 2001. 23

[15] C. S. Hill, et al. *"Initial experience with the CDF layer 00 silicon detector". Nucl. Instrum. and Meth. A* **511** *(2003) 118-120.* 23

[16] A. Sill, et al. Cdf run ii silicon tracking projects. *Nucl. Instrum. and Meth. A* **447** *(200) 1-8.* 23

[17] W. Ashmanskas, et al. The cdf silicon vertex trigger. *Nucl. Instrum. and Meth. A* **518** *(2004) 532-636.* 24

[18] A. Affolder, et al. *"Status report of the Intermediate Silicon Layers detector at CDFII"*, 2001. CDF Public Note 5687. 24

[19] A. Affolder. *"Intermediate silicon layes detector for the CDF experiment". Nucl. Instrum. and Meth. A* **453** *(2000) 84-88.* 24

[20] T. Affolder, et al. *"CDF Central Outer Tracker"*, 2003. CDF Public Note 6267. 25

[21] L. Balka, et al. *"The CDF Central Electromagnetic Calorimeter". Nucl. Instrum. Meth. A* **267***, 272*, 1988. 28

[22] S. Lami, et al. *"The CDF calorimeter upgrade for Run IIb". Nucl. Instrum. Meth. A* **518** *(2004) 39-41.* 29

[23] S. Bertolucci, et al. *"The CDF Central and Endwall Hadron Calorimeter". Nucl. Instrum. Meth. A* **267***, 301*, 1988. 29

[24] Y. Seiya, et al. The cdf plug upgrade electromagnetic calorimeter test beam results. *Nucl. Instrum. Meth. A* **480** *(2002) 524-546.* 29

[25] D. Acosta, et al. *"The CDF Cherenkov luminosity monitor". Nucl. Instrum. Meth. A* **461** *(2001) 540-544.* 32

[26] D. Acosta, et al. *"The performance of the CDF luminosity monitor". Nucl. Instrum. Meth. A* **494** *(2002) 57-62.* 32

[27] *http://www.phys.psu.edu/∼cteq/.* 38

[28] *http://madgraph.hep.uiuc.edu/*. 38

[29] F.Maltoni and T. Stelzer. *"Automatic event generation with MadGraph"*. *JHEP 0303:027*, 2003. 38

[30] Torbjörn Sjöstrand, Stephen Mrenna, and Peter Skands. *"PYTHIA 6.4 Physics and Manual"*. arXiv:hep-ph/0603175. 40

[31] *http://geant4.cern.ch/*. 42

[32] G. Grindhammer and S. Peters. *"The Parameterized Simulation of Electromagnetic Showers in Homogeneous and Sampling Calorimeters"*. arXiv:hep-ph/0001020. 42

[33] Mina Yoshida. "*Multivariate analysis for lepton identification at CDF* ". Master's thesis, Osaka City University, 2010. 43

[34] J. Neyman and E. Pearson. *"On the Problem of the Most Efficient Tests of Statistical Hypotheses"*. *Phil. Trans. of the Royal Soc. Of London*, Vol. 231, p. 289, 1933. 52

[35] Peter Joseph Dong. "Measurement of Electroweak Single Top Quark Production in Proton-Antiproton Collisions at 1.96 TeV". Ph.D. dissertation, University of California, 2008. 52, 75

[36] G. Giurgiu, V. Tiwari, M. Paulini, and J. Russ. *"Muon B Flavor Tagging - A Likelihood Approach"*, 2004. CDF Note 7043. 52

[37] V. Tiwari, G. Giurgiu, M. Paulini, and J. Russ. Likelihood based electron tagging, 2004. CDF Note 7121. 52

[38] *http://tmva.sourceforge.net/*. 73

[39] A. Hoecker, P. Speckmayer, J.Stelzer, J. Therhaag, E. von Toerne, and H.Voss. *"TMVA 4 Toolkit for Multivariate Data Analysis with ROOT Users Guide"*. *CERN-OPEN-2007-007 TMVA version 4.0.3*, 2009. 73

[40] Takayuki Wakisaka. "Search for the Wh Production Using High-p_T Isolated Like-Sign Dilepton Events in 1.96-TeV Proton-Antiproton Collisions". Ph.D. dissertation, Osaka City University, 2009. 73

[41] Juan Cruz Estrada Vigil. "Maximal Use of Kinematic Information for the Extraction of the Mass of the Top Quark in Single-lepton $t\bar{t}$ events at DØ. Ph.D. dissertation, University of Rochester, 2001. 75

[42] Maria Florencia Canelli. "Helicity of the W Boson in Single-Lepton $t\bar{t}$ events". Ph.D. dissertation, University of Rochester, 2003. 75

[43] *http://www.feynarts.de/cuba/*. 79

[44] T. Hahn. *"CUBA - a library for multidimensional numerical integration". Comput.Phys. Commun. 168 (2005) 78.* 79